

Effect of deep convection on the TTL composition over the Southwest Indian Ocean during austral summer.

Stephanie Evan¹, Jerome Brioude¹, Karen Rosenlof², Sean. M. Davis², Holger Vömel³, Damien Héron¹, Françoise Posny¹, Jean-Marc Metzger⁴, Valentin Duflot^{1,4}, Guillaume Payen⁴, Hélène Vérémes¹, Philippe Keckhut⁵, and Jean-Pierre Cammas^{1,4}

¹LACy, Laboratoire de l'Atmosphère et des Cyclones, UMR8105 (CNRS, Université de La Réunion, Météo-France), Saint-Denis de la Réunion, 97490, France

²Chemical Sciences Division, Earth System Research Laboratory, NOAA, Boulder, 80305, CO, USA

³National Center for Atmospheric Research, Boulder, 80301, CO, USA

⁴Observatoire des Sciences de l'Univers de La Réunion, UMS3365 (CNRS, Université de La Réunion, Météo-France), Saint-Denis de la Réunion, 97490, France

⁵LATMOS, Laboratoire ATmosphères, Milieux, Observations Spatiales-IPSL UMR8190 (UVSQ Université Paris-Saclay, Sorbonne Université, CNRS), Guyancourt, 78280, France

Correspondence to: Stephanie Evan (stephanie.evan@univ-reunion.fr)

Abstract. Balloon-borne measurements of CFH water vapor, ozone and temperature and water vapor lidar measurements from the Maïdo Observatory at Réunion Island in the Southwest Indian Ocean (SWIO) were used to study tropical cyclones' influence on TTL composition. The balloon launches were specifically planned using a Lagrangian model and METEOSAT 7 infrared images to sample the convective outflow from Tropical Storm (TS) Corentin on 25 January 2016 and Tropical Cyclone (TC) Enawo on 3 March 2017.

Comparing CFH profile to MLS monthly climatologies, water vapor anomalies were identified. Positive anomalies of water vapor and temperature, and negative anomalies of ozone between 12 and 15 km in altitude (247 to 121hPa) originated from convectively active regions of TS Corentin and TC Enawo, one day before the planned balloon launches, according to the Lagrangian trajectories.

Near the tropopause region, air masses on 25 January 2016 were anomalously dry around 100hPa and were traced back to TS Corentin active convective region where cirrus clouds and deep convective clouds may have dried the layer. An anomalously wet layer around 68 hPa was traced back to the South East IO where a monthly water vapor anomaly of 0.5ppmv was observed. In contrast, no water vapor anomaly was found near or above the tropopause region on 3 March 2017 over Maïdo as the tropopause region was not downwind of TC Enawo. This study compares and contrasts the impact of two tropical cyclones on the humidification of the TTL over the SWIO. It also demonstrates the need for accurate balloon-borne measurements of water

30 vapor/ozone/aerosols in regions where TTL in-situ observations are sparse.

31 **1 Introduction**

32 Deep convection plays an important role in delivering water and other chemical constituents to the Tropical Tropopause Layer
33 (TTL, ~14-19 km altitude, Fueglistaler et al., 2009) and lower stratosphere regions. Two important pathways for trace gas
34 transport from the surface to the tropical stratosphere are i) deep convective injection directly into the stratosphere (Danielsen,
35 1982; Dessler and Sherwood, 2003), ii) convective detrainment into the TTL followed by a slow ascent into the stratosphere
36 (Holton and Gettelman, 2001). Moist boundary layer air is transported to the upper troposphere by deep convection with the
37 main outflow region at about 13 km (Folkins and Martin, 2005). However very deep convection may overshoot the 18 km
38 level into the stratosphere, injecting water vapor and ice crystals directly (Corti et al., 2008; Khaykin et al., 2009; Avery et al.,
39 2017). Studies based on Eulerian cloud resolving models have shown that those overshoots can moisten the lower stratosphere
40 due to evaporation of ice crystals (Dauhut et al., 2015; Frey et al., 2015). However, convection can also cool the cold point
41 tropopause (CPT) (Kuang and Bretherton, 2004), which can enhance dehydration via in-situ formation of cirrus clouds. In fact,
42 the net impact of deep convection on TTL humidity (e.g. moistening versus dehydration) depends on the initial pre-convection
43 TTL relative humidity with respect to ice (RH_i) conditions and size of the ice crystals formed in the convective updrafts (Jensen
44 et al., 2007; Ueyama et al., 2018). In sub-saturated TTL air, condensed ice is not removed quickly enough to produce net
45 dehydration. Recent studies based on Lagrangian models (Schoeberl et al., 2014, Ueyama et al., 2015) that include convection
46 and cirrus clouds microphysics show that convection impacts TTL cirrus clouds and water vapor near the tropical tropopause
47 by 10-30% (~1 ppmv). Therefore, they concluded that convection is significant for the moisture budget of the TTL and must
48 be included to fully model the dynamics and chemistry of the TTL and lower stratosphere.

49 As the exact role of convection in hydrating/dehydrating the stratosphere is still under debate, additional accurate TTL
50 observations and modeling work are still needed to quantify the overall impact of convection on TTL composition and climate.
51 At the moment, a realistic representation of deep convection and its effects remains a challenge for most global scale climate
52 models and numerical weather prediction models (NWP).

53 Our understanding of how deep convection controls TTL humidity and composition, to a large extent, results from experiments
54 in South America, the Western Pacific and South-East Asia (e.g. Toon et al., 2010; Jensen et al., 2017; Brunamonti et al.,
55 2018). The role of the Indian Ocean (IO) in the global climate system is less understood than that of the Pacific Ocean, which
56 has been more intensively observed and studied.

57 The tropical Indian Ocean has seen an unprecedented rise in heat content and is now home to 70% of the global ocean heat

58 gain in the upper 700 m of the ocean during the past decade (Lee et al., 2015). Liu and Zipser (2015) showed using radar
59 observations from the Global Precipitation Measurement (GPM) satellite that deep convection deeper than 15 km (Figure 1 of
60 Liu and Zipser, 2015) can occur over the South IO with dozens of systems reaching above 17 km. These systems are likely
61 tropical cyclones over the SWIO or thunderstorms that are often observed over Madagascar during austral summer (Roca et
62 al., 2002; Bovalo et al.; 2012).

63 Tropical cyclones are unique among tropical and subtropical convective systems in that they persist for many days and hydrate
64 a deep layer of the surrounding upper troposphere (Ray and Rosenlof, 2007). Ray and Rosenlof (2007) used measurements
65 from AIRS to assess the impact of tropical cyclones in the Atlantic and Pacific basins on the amount of water vapor in the
66 tropical UT. They showed that tropical cyclones can hydrate a deep layer of the surrounding upper troposphere by ~30-50
67 ppmv or more within 500 km of the eye compared to the surrounding average water vapor mixing ratios. In addition, a
68 modelling study by Allison et al. (2018) for TC Ingrid (2013) in the Gulf of Mexico indicated overshooting convection within
69 the cyclone and associated strong vertical motions that transported large quantities of vapor and ice to the lower stratosphere.

70 Using 11-year TRMM precipitation satellite observations, Tao and Jiang (2012) identified overshooting tops in tropical
71 cyclones (above 14 km) and showed that the South IO is the second basin after the Northwest Pacific in terms of total number
72 of overshooting tops (cf. Table 2 of Tao and Jiang, 2012). Even though convection occurs predominantly over land in the
73 tropics, overshooting convection in tropical cyclones contributes ~15% of the total convection reaching the tropopause (Romps
74 and Kuang, 2009).

75 The location of Réunion Island (21°S, 55°E) is thus ideal to study tropical cyclone effects on TTL composition. Réunion Island
76 was formally designated as a Regional Specialized Meteorological Centre (RSMC) - Tropical Cyclones for the Southwestern
77 Indian Ocean (SWIO, 0-40°S, 30-100°E) by the World Meteorological Organization (WMO) in 1993. The RSMC Réunion
78 Island is responsible for the monitoring of all the tropical systems occurring over its area of responsibility. **The SWIO is**
79 **the third most active tropical cyclone basin with an average of 9.3 tropical storms with**
80 **maximum sustained winds \geq 63 km/h forming each year (Neumann, 1993).** In the SWIO basin, a storm
81 system is called a tropical cyclone when wind speeds exceed 118 km/h.

82 We take advantage of the position of Réunion Island in the SWIO to study tropical cyclones' influence on TTL composition
83 (water vapor/ozone) during austral summers 2016 and 2017. Austral summer (Nov-March) is the ideal time to sample
84 convective outflow from tropical cyclones or mesoscale convective systems forming near Madagascar.

85 The present work is organized as follows. Section 2 has a description of the data used in this study. Section 3 presents the

86 model used to infer the convective origin of the measurements. Section 4 presents the water vapor/ozone distributions over
87 Réunion Island during the two storm events and thermodynamics of the troposphere and TTL. Section 5 discusses the
88 convective influence on the measurements as inferred from an analysis of Lagrangian trajectories. The results are discussed in
89 Section 6. Section 7 contains a summary of our study.

90 **2 Data**

91 **2.1 Balloon data**

92 Balloon-borne measurements of water vapor and temperature in coordination with ground-based instrumentation (lidars)
93 started in 2014 at the Maïdo Observatory (21.08°S, 55.38°E) within the framework of the Global Climate Observing System
94 (GCOS) Reference Upper-Air Network (GRUAN) network (Bodeker et al., 2016). The balloon sonde payload consists of the
95 Cryogenic Frostpoint Hygrometer (CFH) and the Internet iMet-1-RSB radiosonde for data transmission. The iMet-1-RSB
96 radiosonde provides measurements of pressure, temperature, Relative Humidity (RH) and wind data (speed and direction from
97 which zonal and meridional winds are derived). The CFH was developed to provide highly accurate water vapor measurements
98 in the TTL and stratosphere where the water vapor mixing ratios are extremely low (~2 ppmv). CFH mixing ratio measurement
99 uncertainty ranges from 5% in the tropical lower troposphere to less than 10% in the stratosphere (Vömel et al., 2007b); a
100 recent study shows that the uncertainty in the stratosphere can be as low as 2-3% (Vömel et al., 2016). However, water vapor
101 measurements in the stratosphere by the CFH can be contaminated by sublimation of water from an icy intake, or from the
102 balloon and payload at a pressure lower than 20hPa (Jorge et al., 2020). The iMET-1-RSB has a temperature measurement
103 uncertainty of 0.3°C, or 5% in RH, with an altitude independent bias of 0.5 ± 0.2 °C (Hurst et al., 2011). As for vertical
104 coordinate, we use the geopotential height calculated from the iMet-1-RSB measurements of pressure, temperature and RH.
105 Hurst et al. (2011) reported altitude-dependent differences of -0.1 to -0.2 km above 20 km between the geopotential altitudes
106 derived from the Vaisala RS92 and Internet iMet-1-RSB sondes. The CFH and iMet-1-RSB measurements have high vertical
107 resolution (5-10m) and are binned in altitude intervals of 200 m to reduce measurement noise. Here we present CFH
108 measurements (water vapor mixing ratio and Relative Humidity with respect to ice, RH_{ice}) from 2 soundings performed in
109 austral summers 2016 and 2017, when deep convection was active near Réunion Island (tropical cyclones Corentin and Enawo,
110 cf. Figure 1). During austral summer, balloon launch planning is optimized using a Lagrangian forecasting tool. 5-day
111 backward Lagrangian trajectories initialized from the location of the Maïdo Observatory at different altitudes (9.5, 12.5, 15.5
112 and 18 km) are run twice-daily and superimposed on current geostationary infrared satellite images to identify on-going
113 convection over the SWIO (<http://geosur.univ-reunion.fr/foot>). This allows the identification of air masses with a convective
114 origin that can be measured at the Observatory, thereby maximizing local resources by only measuring when convectively

115 influenced air masses will be sampled.

116 In addition to CFH measurements at the Observatory, weekly Network for the Detection of Atmospheric Composition Change
117 (NDACC)/Southern Hemisphere ADditional OZonesondes (SHADOZ) ozonesondes (Thompson et al., 2003; Witte et al.,
118 2017) are launched from the airport (Gillot: 21.06°S, 55.48°E), located on the north side of the island (the flying distance
119 between the Maïdo Observatory and the airport is ~20km). The ozonesonde is flown with a Meteomodem M10 radiosonde
120 that provides meteorological variables such as temperature, pressure, relative humidity and winds. In this study, the
121 NDACC/SHADOZ ozone and temperature measurements are reported in 200 m altitude bins.

122 **2.2 Water vapor lidar data**

123 A Raman water vapor lidar emitting at 355 nm has been operating at the Maïdo Observatory since April 2013 (Baray et al.,
124 2013; Keckhut et al., 2015; Vèrèmes et al., 2019). Laser pulses are generated by two Quanta Ray Nd:Yag lasers, the geometry
125 for transmitter and receiver is coaxial and the backscattered signal is collected by a Newtonian telescope with a primary mirror
126 of 1200 mm diameter. 387 nm (N₂) and 407 nm (H₂O) Raman shifted wavelengths are used to retrieve the water vapor mixing
127 ratio. Depending on the scientific investigations, specific filter points and integration times can be chosen. The raw vertical
128 resolution is 15 m. Data are smoothed with a low-pass filter using a Blackman window. Based on the number of points used
129 for this filter to vertically average the data, the vertical resolutions are 100-200 m in the lowest layers, 500 m in the mid-
130 troposphere, 600 m in the upper troposphere and 700-750 m in the lower stratosphere. In order to convert the backscattered
131 radiation profiles into water vapor mixing ratio profiles, the calibration coefficient is calculated from water vapor column
132 ancillary data: GNSS (Global Navigation Satellite System) IWV (Integrated Water Vapor). The description of the calibration
133 method and the total uncertainty budget can be found in Vèrèmes et al. (2019).

134 At the Maïdo Observatory, the lidar provides 4 to 8 water vapor profiles per month. The calibrated lidar water vapor
135 database extends from November 2013 to December 2017. The time slot of routine operations is around 19:00 to 01:00 (+1)
136 local time but there are intensive periods of observation during field campaigns that allow longer measuring span. The Raman
137 lidar water vapor observations were validated during the Maïdo ObservatoRy Gaz and Aerosols NDACC Experiment
138 (MORGANE) intercomparison exercise in May 2015 (Vèrèmes et al., 2019). During the MORGANE campaign, CFH
139 radiosonde and Raman lidar profiles showed mean differences smaller than 9 % up to 22 km asl.

140 Here we used the Raman lidar measurements for two nights when the CFH sondes were launched at the Observatory (25
141 January 2016 and 3 March 2017). The lidar water vapor profiles correspond to an integration time of 239 min and 184 min for
142 the nights of 25 January 2016 and 3 March 2017 respectively. The lidar water vapor profiles are interpolated to the same 200-
143 m vertical grid used for the CFH data and are shown up to 14.5 km. The mean lidar uncertainties for the troposphere below
144 this level are 10.5% and 8.7% for 25 January 2016 and 3 March 2017 respectively.

145 **2.3 Satellite data**

146 The brightness temperatures of the infrared (IR) channel at 10.8 μm of the geostationary weather satellite METEOSAT-7 have
147 been used to provide the regional characteristics of deep convection over the Indian Ocean. The satellite centered at 57.5°E
148 provided images for the Indian Ocean from December 2005 to March 2017.

149 Aura Microwave Limb Sounder (MLS) v4.2 water vapor and ozone data were included in the study to compare with the in
150 situ measurements and to evaluate the spatial extent of the convective air masses measured at the Observatory. In particular
151 we have used water vapor from the Stratospheric Water and OzOne Satellite Homogenized (SWOOSH) data set (Davis et al.,
152 2016). The SWOOSH dataset contains monthly mean stratospheric water vapor and ozone profiles from several satellite
153 instruments for the period 1984 to present. The data are available on a 3D (longitude/latitude/pressure) grid. The SWOOSH
154 input data for the period August 2004 to present day correspond to measurements from the Aura MLS satellite. The MLS water
155 vapor data are available on a pressure grid with 12 levels per decade change in pressure between 1000 and 1 hPa (e.g. the
156 vertical resolution is ranging from 1.3 to 3.6 km between 316 and 1 hPa). The estimated accuracy for MLS water vapor
157 decreases from 20% at 216 hPa to 4% at 1 hPa and is $\sim 10\%$ in the TTL region (150-70 hPa).

158 Cloud-Aerosol Lidar with Orthogonal Polarization (CALIOP) onboard Cloud Aerosol Lidar and Infrared Pathfinder Satellite
159 Observation (CALIPSO) makes backscatter measurements at 532 nm and 1064 nm since June 2006. We use the Total
160 Attenuated Backscatter coefficients β'_{532} available from the CALIPSO V4.10 level 1 lidar data products. Following Vaughan
161 et al. (2004), the attenuated scattering ratio SR_{532} (Equation 3 of Vaughan et al., 2004) profiles are computed as the ratio of
162 β'_{532} corrected for molecular attenuation and ozone absorption and the molecular backscatter coefficient β_m . β_m is calculated
163 using the number density of molecules from the GEOS 5 global model of the NASA Global Modeling and Assimilation Office
164 (GMAO) and the Rayleigh scattering cross section. More details are given in the CALIOP Algorithm Theoretical Basis
165 Document (ATBD, cf. Equations 4.13a and 4.14).

166 **2.4 Model**

167 The origin of air masses measured at the Maïdo Observatory were assessed using the FLEXible PARTicle (FLEXPART)
168 Lagrangian Particle Dispersion Model (Stohl et al., 2005). FLEXPART is a transport model that can be run either in forward
169 or backward mode in time. FLEXPART was driven by using ECMWF analysis (at 00, 12 UTC) and their hourly forecast fields
170 from the operational European Centre for Medium Range Weather Forecasts - Integrated Forecast System (ECMWF-IFS). In
171 March 2016, ECMWF introduced a new model cycle of the IFS into operations with a grid-spacing of 9 km roughly doubling
172 the previous grid-spacing of 16 km used since January 2010. The ECMWF model has 137 vertical model levels with a top at
173 0.01 hPa since June 2013. To compute the FLEXPART trajectories, the ECMWF meteorological fields were retrieved at 0.50°

174 and 0.15° and on full model levels from the Meteorological Archival and Retrieval System (MARS) server at ECMWF. The
175 0.50° fields were used to drive the FLEXPART model over a large domain configured as a tropical channel, i.e., the domain
176 is global in the zonal direction but bounded in the meridional direction (at latitudes $\pm 50^\circ$). Furthermore, higher-resolution
177 domains can be nested into a mother domain in a FLEXPART simulation. Thus, to have a better representation of convective
178 transport associated with mesoscale convective systems or tropical cyclones with a horizontal dimension on the order of a
179 couple of hundred kilometers over the SWIO, we included a nest domain covering the SWIO region (20°E - 80°E , 40°S - 10°N).
180 If a particle resides in the high-resolution nest, the ECMWF meteorological data at 0.15° from this nest are interpolated linearly
181 to the particle position. If not, the $0.50 \times 0.50^\circ$ ECMWF meteorological data from the mother domain are used to compute the
182 trajectories. Retrieving high-resolution ECMWF fields from the MARS server for FLEXPART consists in several steps which
183 are:

- 184 - retrieve the meteorological model data output from ECMWF (horizontal winds, temperature, humidity, surface fields)
- 185 - compute total and convective precipitation rates, sensible and latent heat fluxes from the surface
- 186 - calculate the vertical velocity from the continuity equation

187 Therefore, the ECMWF high-resolution vertical velocity field already contains a convective mass flux component from the
188 Tiedtke scheme used in ECMWF. The convective scheme used in the ECMWF-IFS, originally described in Tiedtke (1989),
189 has evolved over time. Changes made include a modified entrainment formulation leading to an improved representation of
190 tropical variability of convection (Bechtold et al. 2008) and a modified CAPE closure leading to a significantly improved
191 diurnal cycle of convection (Bechtold et al. 2014). Particles are transported both by the resolved winds and parameterized sub-
192 grid motions, including a vertical deep convection scheme. FLEXPART uses the convective parameterization by Emanuel and
193 Zivkovic-Rothman (1999) to simulate the vertical displacement of particles due to convection. The results from model runs
194 with and without cumulus scheme in FLEXPART have been compared to assess whether convective mass fluxes could be
195 resolved in the higher-resolution nest domain. The results of FLEXPART runs with and without cumulus scheme look fairly
196 similar (not shown) and thus here we will present only the model results with cumulus scheme turned off.

197 To determine the transport history of air masses sampled by balloon launches, a so-called retroplume was calculated consisting
198 of 10,000 back trajectory particles released from each 1 km layers of balloon launches used in this study, and advected
199 backward in time. The initial positions of the 50,000 particles were distributed randomly within 19 vertical layers
200 (corresponding to the MLS pressure levels between 316 and 10 hPa) with a depth of 1 km and $0.10^\circ \times 0.10^\circ$ longitude-latitude
201 bins centered on the balloon location. The dispersion of a retroplume backward in time indicates the likely source regions of
202 the air masses sampled by the in situ instruments.

203 **3 Tropical storm Corentin (January 2016) and tropical cyclone Enawo (March 2017).**

204 **3.1 Convective activity**

205 Figure 1 shows the best tracks (i.e. a smoothed representation of the tropical cyclone's location over its lifetime, red line on
206 each panel of Figure 1) of Tropical Storm (TS) Corentin and Tropical Cyclone (TC) Enawo. The best track represents the best
207 guess of the location of the tropical cyclone center every 6 hours. TS Corentin started to form on 19 January 2016, east of
208 70°E. The METEOSAT 7 IR brightness temperatures on 19 January 2016 at 11 UTC indicate a vast clockwise circulation with
209 some organization (not shown), indicative of tropical cyclone formation in the SH. The strengthening of the northerly monsoon
210 flow favored the deepening of the system in the subsequent days. Corentin became a moderate tropical storm (10-min
211 maximum sustained wind speeds of 65 km/h) on 21 January 2016 at 00 UTC and at that time the TS center was located at
212 14.93°S, 75.63°E, ~2200 km to the northeast of the island. TS Corentin continued to intensify on January 22 while moving
213 towards the south (see best track on Figure 1). TS Corentin reached its peak intensity on January 23 at 00 UTC with 10-minute
214 maximum sustained wind speeds of 110 km/h and the pressure at the center was 975 hPa. On 23 January 2016, convection was
215 strong around 10°S in the Mozambique Channel and near TS Corentin, especially in the northern part of the system. On January
216 24, Corentin had weakened into a moderate tropical storm. On 25 January at 18 UTC (time of the balloon launch at the Maïdo
217 Observatory), the storm was located at about 2500 km southeast of Réunion Island, near 26.03° south latitude and 79.19° east
218 longitude (Figure 1).

219 The Madden Julian Oscillation (MJO) was active at the end of February and during the first week of March 2017 with a signal
220 centered over Africa and the Indian Ocean. A monsoon trough was well defined all over the basin along 9°S. On 28 February
221 2017 at 10 UTC, a zone of disturbed weather formed around 6.5°S, 70.2°E (not shown) with the building of clockwise rotating
222 movement inside the cloud pattern. Favored by the MJO active phase and the arrival of an equatorial Rossby wave, Enawo
223 initially formed as a tropical disturbance on March 2 with 10-minute maximum sustained wind speeds ~ 40 km/h. Enawo
224 intensified to a moderate tropical storm at 06:00 UTC on March 3. At the time of the balloon launch at the Observatory (~3
225 March, 18 UTC), Enawo was a tropical storm located near 13° south latitude and 56.42° east longitude, about 900 km north-
226 northwest of Réunion Island (Figure 1). It strengthened into a severe tropical storm cyclone on 5 March at 00 UTC and became
227 a category 1 tropical cyclone at 12 UTC. TC Enawo continued to intensify while moving toward Madagascar. It became a
228 category 4 tropical cyclone on March 6 at 18:00 UTC, with 10-minute maximum sustained winds at 194 km/h. Enawo reached
229 its peak intensity at 06:00 UTC on March 7, with ten-minute maximum sustained winds at 204 km/h and the central pressure
230 at 932 hPa. TC Enawo reached Madagascar's northeastern coast on March 7 at around 9:30 UTC and was the third strongest
231 tropical cyclone on record to strike the island. After March 8, TC Enawo gradually weakened to a tropical storm while moving
232 southward over Madagascar.

233 The two balloon launches at the Observatory on 25 January 2016 and 3 March 2017 were specifically planned using
234 FLEXPART Lagrangian trajectories and METEOSAT 7 infrared images. The goal was to sample the convective outflow from
235 TS Corentin and TC Enawo as well as convection north of Madagascar on 24 January 2016.

236 To assess the potential effects of deep convection in the upper troposphere and near the tropopause, we looked at the
237 distribution of deep convective clouds in the days preceding the soundings. The location of deep convective clouds can be
238 assessed by using maps of METEOSAT 7 infrared brightness temperature. Figure 2 shows convective cloud coverage for the
239 3-day period preceding the sonde launch date at the Maïdo Observatory. Convective cloud coverage was estimated using 3-
240 hourly METEOSAT 7 infrared brightness temperatures at 5 km resolution. A threshold of 230 K is used to detect deep
241 convective clouds in the METEOSAT 7 brightness temperature data (i.e. pixels with brightness temperatures less than 230 K
242 correspond to convective clouds). This threshold has been previously used to identify convection on geostationary satellite
243 infrared images (e.g. Tissier et al., 2016). This temperature corresponds to a height of about 11 km in the NDACC/SHADOZ
244 climatological-mean summertime profile of temperature. Prior to 25 January 2016, the main deep convective activity is located
245 ~1500 km north of the island between 50 and 70°E and around tropical storm Corentin. From 28 February to 3 March 2017,
246 convective clouds are located ~500 km north of the island and correspond to the intensifying tropical storm Enawo. The coldest
247 cloud tops (≤ 190 K) that correspond to the deepest convection are indicated by red dots on Figure 8.

248 **3.2 Monthly mean water vapor distributions.**

249 Figures 3 show MLS water vapor volume mixing ratios at 215 hPa and 100 hPa averaged over January 2016 and March 2017.
250 These values were computed by averaging the SWOOSH monthly mean water vapor concentrations gridded on a regular
251 pressure/latitude/longitude (resolution of $5^\circ \times 20^\circ$) grid.

252 When comparing the water vapor mixing ratio at 215 hPa in January 2016 to the one observed in March 2017, one can see that
253 the upper troposphere over the SWIO was much moister in January 2016 than in March 2017 with three distinct regions of
254 enhanced water vapor over Central Africa, the Indian Ocean and the Maritime Continent. The mean water vapor mixing ratio
255 at 215 hPa over the SWIO in January 2016 is greater by ~23 ppmv compared to March 2017. Interannual variability modes
256 such as the El-Niño–Southern Oscillation (ENSO) can affect the TTL temperature, and thus, water vapor distribution. The
257 NOAA Climate Prediction Center Ocean Niño index (ONI), which is based on SST anomalies in the Niño 3.4 region, was
258 equal to +2.5 K in January 2016 versus +0.1 K in March 2017
259 (http://origin.cpc.ncep.noaa.gov/products/analysis_monitoring/ensostuff/ONI_v5.php). January 2016 corresponded to strong
260 El Niño conditions (one of the strongest El Niño event since 1950 according to the ONI index) while March 2017 was
261 associated with neutral ENSO conditions. The water vapor mixing ratios at 215 hPa for January 2016 are in agreement with

262 MLS DJFM climatological values of water vapor at 215 hPa for El Niño conditions (not shown). Overall during El Niño
263 conditions, water vapor mixing ratios at 215 hPa are enhanced over the SWIO west of 80°E. Ho et al. (2006) have studied the
264 variations of TC activity in the South Indian Ocean in relation to ENSO effects. During El Niño periods TC genesis was shifted
265 westward, enhancing the formation west of 75°E and reducing it east of 75°E. Therefore, on January 2016 the peak of water
266 vapor west of 80°E at 215 hPa may be related to an increase in convection associated with strong El Niño conditions.

267 The Quasi-Biennial Oscillation (QBO) also affects TTL temperatures and humidity (e.g. Zhou et al., 2001; Yuan et al., 2014;
268 Davis et al., 2013). Following Davis et al. (2013), we defined a QBO index as the zonal mean (10°S-10°N) of the difference
269 in the ERA-Interim zonal wind at 70 and 100 hPa. A positive QBO index ($u_{70\text{hPa}} - u_{100\text{hPa}} > 0$) corresponds to westerly shear
270 conditions and the warm phase of the QBO (Baldwin et al., 2001). A negative QBO index corresponds to easterly shear
271 conditions and the cold phase of the QBO (CPT temperatures are cooler during the easterly shear phase of the QBO). The
272 mean January 2016 water vapor mixing ratio at 100 hPa over the SWIO is 4.2 ppmv versus 3.7 ppmv in March 2017 as
273 compared to the climatological values of 3.51 ppmv for January and 3.44 ppmv of March. The difference of 0.50 ppmv between
274 the two periods cannot be explained by the phase of the QBO as both months corresponded to QBO westerly shear conditions
275 (2.33 m/s for January 2016 and 4.79 m/s for March 2017). However, the higher water vapor mixing ratio at 100 hPa in January
276 2016 could be related to strong El Niño conditions as Avery et al. (2017) have reported large lower stratospheric (82 hPa)
277 water vapor anomalies ($\sim +0.9$ ppmv) associated with the strong 2015-2016 El Niño. The highest SWOOSH water vapor
278 mixing ratio anomalies of $\sim +1$ ppmv were observed over the Indian Ocean in December 2015 (not shown). In January 2016,
279 the anomalies over the SWIO have eased to 0.7 ppmv (not shown).

280

281 **4. Observations**

282 **4.1 Water vapor/ozone profiles**

283 Figure 4 shows two CFH water vapour mixing-ratio profiles (black lines) taken at the Maïdo Observatory on 25 January 2016
284 at 17:50 UTC and 3 March 2017 at 18:00 UTC. The lidar water vapor profiles for those two nights are also displayed in green.
285 The red and purple lines correspond to NDACC/SHADOZ ozonesonde balloon profiles launched from Gillot on 18 January
286 2016 (purple line), 4 February 2016 (red line) and 3 March 2017 (purple line on the right panel). The ozonesonde data
287 correspond to daytime measurements (balloon launches at ~ 11 UTC) while the CFH water vapor data correspond to nighttime
288 measurements in order to coincide with water vapor lidar measurements at the Maïdo Observatory. Overall good agreement is
289 seen between the lidar and CFH water vapor profiles over the whole troposphere. Note that the CFH water vapor profiles were
290 not used to calibrate the lidar water vapor profiles as explained in section 2.2.

291 The altitude range 2-12 km on 25 January 2016 is moister by ~50% than the same altitude range on 3 March 2017 (mean water
292 vapor mixing ratio of 5076 ppmv and 4375 ppmv between 2 and 12 km on 25 January 2016 for the CFH and lidar respectively
293 versus 3335 ppmv and 3398 ppmv on 3 March 2017 for the CFH and lidar respectively). The austral summer season, with
294 warmer temperatures and greater cloudiness, reaches its peak in January/February and this could explain in part the higher
295 humidity observed in January than March. In addition, January 2016 corresponded to a strong El Niño period and this could
296 lead to higher tropospheric moistening associated with ENSO (Tian et al., 2019). On 3 March 2017, a moist layer was observed
297 between ~12 and 16 km in both CFH and lidar water vapor profiles with corresponding low ozone values (Figure 4, right). On
298 25 January 2016, two local moist layers around 10 and 15 km associated with low ozone are observed. The lidar smooths out
299 the peak of water vapor at 10 km observed on 25 January 2016 but this could be due to the longer integration time used for
300 that night (239 min). The CFH water vapor mixing ratio profiles have a minimum of 2.5 ppmv at 17.10 km (94 hPa) and 2.70
301 ppmv at 18.10 km (77.1 hPa) on 25 January 2016 and 3 March 2017 respectively.

302 Also shown is the climatological mean ozone profile for DJFM 1998-2017 (blue lines on Figure 4). Anomalously low mixing
303 ratios approaching surface values are seen in the upper troposphere for both the 4 February 2016 (red line, Fig. 4a) and 3 March
304 2017 (purple line, Fig. 4b) ozone sonde flights. In the upper troposphere, the climatological mean ozone mixing ratios ranges
305 from about 60 ppbv at 10 km to 100 ppbv at 15 km. There is a steep gradient above 17 km, indicating the transition from
306 troposphere to stratosphere. On 3 March 2017, ozone mixing ratios between 10 and 15 km are ~ 45 ppbv below the
307 climatological values (mean value of 25.10 ppbv for the 10-15 km layer on 3 March 2017 versus 70.1 ppbv for the
308 climatological ozone profile).

309 Between 18 January and 4 February 2016, ozone mixing ratios in the upper troposphere decreased by ~30 ppbv and are 38
310 ppbv below the climatological values on 4 February 2016. Tropical storm Corentin reached its peak intensity on 23 January
311 2016 at 00 UTC and its center was located 1735 km east of Réunion Island. These low ozone mixing ratios in the upper
312 troposphere on 4 February 2016 were observed after the storm had its major influence on UT ozone, transporting air with
313 surface ozone values upward via strong convection and mixing out into the larger environment. In comparison, the 18 January
314 2016 ozone profile was not influenced by TS Corentin. The lower ozone values on 3 March 2017 compared to those observed
315 on 4 February 2016 could be explained by the fact that TC Enawo was closer to the island (~902 km north of the island), was
316 still intensifying and was a stronger system than TS Corentin. Above ~17 km the ozone profiles in January/February 2016 and
317 March 2017 are more similar to the climatological mean ozone profile, suggesting that deep convection did influence the upper
318 troposphere but not the lower stratosphere. We will later show using FLEXPART that the moist/low ozone layers in Figure 5
319 are associated with the convective outflow of a mesoscale convective system north of Madagascar on 23 January 2016, TS
320 Corentin and TC Enawo.

321 4.2 Relative humidity and temperature profiles

322 Figure 5 shows the CFH profiles of RH_{ice} (computed using the Goff-Gratch equation [Goff and Gratch, 1946] for water vapor
323 pressure) on 25 January 2016 and 3 March 2017 as well as collocated CALIOP nighttime backscatter measurements. The
324 CALIOP measurements shown on Figure 5 include only those within $\pm 5^\circ$ latitude and $\pm 10^\circ$ longitude of the Maïdo
325 Observatory. The CALIOP measurements on 25 January 2016 correspond to a CALIPSO overpass east of the island around 4
326 hours after the balloon launch and the mean longitude difference between the CALIPSO overpass and the Maïdo Observatory
327 is 2.4° for Figure 5-top. On 3 March 2017, the CALIPSO overpass was west of the island and also 4 hours after the balloon
328 launch. The mean longitude difference between the CALIPSO overpass and the Maïdo Observatory is 5.3° . The latitude-height
329 cross-section of CALIOP SR_{532} on Figure 5 corresponds to measurements with a 60 m vertical resolution. The horizontal
330 interval of the CALIOP data along its orbit is 330 m; for this study we use a 9-point running average to reduce noise.

331 Figure 5 (top) shows significant structure in the RH_{ice} profile measured on 25 January 2016. Higher values of RH_{ice} ($> 40\%$)
332 between 13 and 15 km coincide with higher values of CALIOP SR_{532} between 12 and 15 km. The RH_{ice} reaches its maximum
333 value at the coldpoint altitude (17.3 km). The CALIOP SR_{532} indicates a cirrus cloud between ~ 12 and 15 km north of the
334 island. The cirrus layer extends from $\sim 16.2^\circ S$ to $20^\circ S$ corresponding to a horizontal scale of ~ 400 km. METEOSAT 7 infrared
335 brightness temperature at 21:30 UTC, so ~ 10 minutes before the CALIPSO overpass at 21:39 UTC on Figure 5 (top), indicates
336 a large area of deep convection near $15^\circ S$ and extending from $\sim 50^\circ$ to $75^\circ E$ (not shown). The monsoon trough was located
337 between $17^\circ S/50^\circ E$ and $14^\circ S/70^\circ E$ on 25 January 2016 which promoted deep convection and convective activity was also
338 observed in the South-Eastern quadrant of TS Corentin. The cirrus cloud observed below 15 km on Figure 5 (top) was most
339 likely from convective detrainment north of Réunion Island. The RH_{ice} profile on January 25 indicates intertwined layers of
340 dry air (RH_{ice} less than 40%) at 7, 9, 12 and 16 km and less dry air ($RH_{ice} \sim 50\%$) at 8, 11, 15 and 17 km. While convection
341 north of Réunion Island around $15^\circ S$ and TS Corentin had mixed the troposphere over the Southwest Indian Ocean, no cirrus
342 clouds were directly observed on 25 January 2016 above the Maïdo Observatory. The layers of $RH_{ice} \sim 50\%$ at 15 and 17 km
343 may be due to convective detrainment. The cirrus cloud below 15 km detected by CALIPSO north of the island on January 25
344 indicates that deep convection detrained ice and water vapor in the upper troposphere north of the island. There was a northerly
345 wind between 10 and 17 km on 25 January 2016 with a peak around -25 m s^{-1} at 15 km (cf. Figure 1). Moist air detrained by
346 deep convection north of Réunion near $15^\circ S$ may have been transported to Réunion Island in ~ 6 hours and during that time
347 the moist air mass could have mixed with drier air, thereby explaining the layers of $RH_{ice} \sim 50\%$ at 15 and 17 km on Figure 5.
348 The origin of these layers has also been determined using the FLEXPART Lagrangian model, and the results are presented in
349 the next section.

350 On 3 March 2017, a layer close to saturation ($RH_{ice} > 80\%$) can be observed between 12 and 16 km (Figure 5, bottom left)

351 with RH_{ice} up to $\sim 100\%$ at 12.5 and 14 km, below the coldpoint altitude (16.1 km). The altitude range 12-15.5 corresponds to
352 cloudy air and a cirrus cloud can be seen in the CALIOP measurements of SR_{532} between ~ 13 and 15 km extending from
353 $18.4^{\circ}S$ to $21.2^{\circ}S$ (Fig 6, bottom right). Above Réunion Island, the cirrus is ~ 1.5 km thick and the maximum thickness of ~ 3
354 km is observed north of the island at $20.5^{\circ}S$. A second cirrus cloud can also be observed below 15 km north of $17.4^{\circ}S$.

355 The CPT height is 16.10 km on 3 March 2017 while it is 1.2 km higher on 25 January 2016 (Figure 5). The CPT temperature
356 was 192.64 K on 25 January 2016 and 194.58 K on 3 March 2017. On 3 March 2017, the layer between 16 and 18 km is almost
357 isothermal with a mean temperature of 195 K while the tropopause is sharper on 25 January 2016.

358 **4.3 Lagrangian analysis**

359 The convective origin of air masses sampled in the upper troposphere and near the tropopause during the passage of TS
360 Corentin and TC Enawo is evaluated using the FLEXPART Lagrangian model. Figure 6 presents the origins of air masses
361 sampled within layer L1 (12.1-13.1km, ~ 178 hPa) and layer L2 (16.3-17.3km, ~ 100 hPa), altitudes that correspond to RH_i peaks
362 on Figure 5 on January 25 2016 above the Maïdo Observatory. The origins and pathways of these air masses were examined
363 by computing 10-day FLEXPART back trajectories. On Figure 6, the origins of air masses measured in the upper troposphere
364 (layer L1) and near the tropopause (layer L2) are shown for two day and three days prior to the launch. The position of each
365 air mass is depicted by 10,000 dots color coded by their altitude and is overlaid over METEOSAT 7 infrared images valid at
366 the time of the back trajectories. For example, trajectories that were originally in the lower troposphere (below 5 km) and
367 middle troposphere (between 5 and 10 km) two/three days before are indicated by orange and brown dots respectively. In
368 other words, these air masses were transported from the troposphere to the upper-troposphere/tropopause region in two or three
369 days before being sampled by the CFH instrument on 25 January 2016 around 18:30 UTC above the Maïdo Observatory. The
370 air mass fractions for different altitude ranges are also indicated at the bottom of Figure 6. Variations in the air mass fractions
371 over time (e.g. from the lower troposphere below 5 km) can be interpreted in terms of changes in the vertical transport due to
372 convection over the SWIO.

373 The ability of FLEXPART to represent isolated deep convective cells is limited, due to the $0.15^{\circ} \times 0.15^{\circ}$ spatial resolution of
374 the ECMWF operational fields. At that resolution, isolated deep convective cells are not fully resolved in the ECMWF vertical
375 wind field, and their updraft intensity and the altitude of the level of neutral buoyancy could be underestimated. However, the
376 vertical transport of convective cells organised at mesoscale such as convection in tropical cyclones that cover several degrees
377 in longitude and latitude are better resolved by the $0.15^{\circ} \times 0.15^{\circ}$ ECMWF meteorological fields. Recent improvements of the
378 ECMWF IFS model have enhanced its forecasting skills of tropical cyclones (Magnusson et al., 2019). Hence the FLEXPART
379 backtrajectories driven by the ECMWF operational wind field give a qualitative sense of convective origins of vertical layers

380 measured at Maïdo in relation to tropical cyclones.

381 According to FLEXPART, layer L1 measured above the Maïdo Observatory on 25 January 2016 ~18:30 UTC has two different
382 origins. Two days before (Figure 6, top left), 48% of this air mass was below 10 km (with ~31% below 5 km) and ~1000 km
383 northeast of Réunion Island in a region with convective clouds with cold brightness temperatures less than 220 K (~12 km).
384 Therefore, we can infer that the majority of the layer L1 was lifted by convection associated with TS Corentin two days prior
385 to the launch. These trajectories are rather spread in the lower troposphere, suggesting that they experienced turbulent mixing
386 and changes in wind direction in the lower troposphere. The rest of the trajectories are located higher in altitude, in the 10-15
387 and 15-17 km altitude ranges. They are also located above convective clouds but are less scattered than the trajectories in the
388 lower troposphere, suggesting that these trajectories were less mixed with the surrounding upper troposphere.

389 Three days before (Figure 6, top right), 66% of layer L1 originated from the lower and middle troposphere (41% within the 0-
390 5 km layer, 25% within the 5-10 km layer) over the northeastern convective region of TS Corentin, and 32% from the upper
391 troposphere (within 10-15 km) above TS Corentin. The upper tropospheric branch had an anticlockwise rotation with an origin
392 near TS Corentin, in agreement with the upper divergence associated with TS Corentin. Hence, most of the air mass was
393 located either in the lower troposphere or near the top of convective clouds three days before.

394 Layer L2 measured at Maïdo on 25 January 2016 stayed in the upper troposphere and near the tropopause two days before
395 reaching Réunion Island (figure 6, bottom left). The trajectories followed an anticlockwise rotation associated with Corentin's
396 dynamics and were located ~250 km north of the center of TS Corentin. Only 3% of trajectories that originate in the lower
397 troposphere were found. On 22 January at 17 UTC (three days before the launch), the trajectories were located East of the
398 center of Corentin (Figure 6, bottom right). About 8% of the trajectories were below 10km (6.4% below 5km). Note that TS
399 Corentin reached its peak intensity on 23 January 2016 at 06 UTC (pressure at the center of 975 hPa, ten-minute maximum
400 sustained winds of 110 km/h). Hence, according to FLEXPART backtrajectories and the METEOSAT 7 infrared images, the
401 origin of layer L2 was traced back to the active convective regions of TS Corentin and its upper divergence dynamics, but a
402 small fraction originated from the lower troposphere. However, due to the 0.15° spatial resolution of the ECMWF winds used
403 to drive FLEXPART, the vertical updrafts of the deepest convective clouds that may reach the tropopause region/lower
404 stratosphere may not be well represented in FLEXPART.

405 Figure 7 is similar to Figure 6 but for backtrajectories associated with the launch on 3 March 2017. Most of the layer L4
406 measured on 3 March 2017 at 18:42UTC was lifted by convection 800 km north of the island two to three days before (Figure
407 7 top). Two days before (Figure 7, top left), the backtrajectories indicate that a large fraction (69%) of layer L4 is from the
408 lower troposphere (below 10 km) over a convective region associated with TC Enawo. Three days before reaching Réunion

409 Island (Figure 7 top right), the trajectories were dispersed in the lower troposphere around the forming storm as Enawo was in
410 the early stage of its formation at that time (tropical depression).

411 The FLEXPART backtrajectories for layer L5 measured above the Maïdo Observatory on 3 March 2017 at 18:52 UTC stayed
412 in the upper troposphere two and three days before the launch (Figure 7 bottom). The trajectories were confined to the same
413 latitude band east and west of Réunion Island in a clear sky region, away from convective clouds. It shows that air masses near
414 the tropopause above Réunion Island on 3 March 2017 were most likely not affected by Enawo at this stage of its development
415 as Enawo was still intensifying.

416 In a nutshell, the FLEXPART backtrajectories clearly identify a convective origin for layers L1 and L4 sampled on 25 January
417 2016 and 3 March 2017 associated with TS Corentin and TC Enawo tropical cyclones. The convective transport from the lower
418 troposphere to the upper troposphere occurred roughly two days before each launch. As for the tropopause region over Réunion
419 Island on 25 January 2016, FLEXPART backtrajectories suggest that the air masses were embedded in TS Corentin upper
420 divergence dynamics over a region where convection was active. Deep convective clouds within TS Corentin may have
421 reached the tropopause region (layer L2) on 23 January 2016 when the storm was at its peak intensity and may have influenced
422 the water vapor content near the tropopause. On 3 March 2017, the tropopause region measured by the CFH sounding was not
423 affected by deep convection associated with Enawo according to the model, at least not at the time of the observation. At that
424 time, TC Enawo was still intensifying and the deepest convective cloud developed later after 4 March 2017.

425

426 **5. Discussion**

427 **5.1 CFH and MLS comparisons**

428 The CFH measurements analyzed in this study are compared to coincident MLS profiles. The match criteria used are ± 18 h,
429 ± 500 km North-South distance (around $\pm 5^\circ$ latitude), ± 1000 km East-West distance (around $\pm 10^\circ$ longitude). The same match
430 criteria are used in Davis et al. (2016). In addition, FLEXPART backtrajectories initialized at each MLS pressure levels are
431 used to isolate the MLS profiles that were originating from TS Corentin and TC Enawo. 5 and 3 matched MLS profiles are
432 found for 25 January 2016 and 3 March 2017 respectively. On 25 January 2016, distances between the Maïdo Observatory
433 and the matched MLS profiles range from 259 to 494 km, with a mean distance of 346 km. The mean time difference for all
434 matched profiles is 3.7 h. On 3 March 2017, the 3 matched MLS profiles are closer to the Maïdo Observatory with a mean
435 distance of 281 km and are east of the island. However, a larger mean time difference of 16.4 h is observed for the matched
436 MLS profiles.

437 To compare the high-resolution CFH water vapor profile to the MLS satellite data, we smooth the high resolution sonde
438 measurements to match the resolution of the satellite profiles using the MLS vertical averaging kernels, following the
439 procedure described in Read et al. (2007) and Davis et al. (2016). The procedure for applying the MLS averaging kernels to a
440 CFH profile requires an a priori profile as input; this is the same a priori profile used in the MLS retrieval. Figure 8 shows the
441 matched MLS profiles and the CFH profiles convolved with the MLS averaging kernels. The matched MLS profiles on both
442 dates illustrate how water vapor is more variable in the upper troposphere (between 316 and ~147 hPa) compared to above.
443 The lower part of the tropopause layer from 147 hPa to the cold point tropopause (green dashed line on Figure 8) is a transition
444 region where water vapor mixing ratios become lower but could still be influenced by deep convective outflow. The application
445 of the averaging kernel to the CFH profiles smoothes the fine-scale structures observed in the CFH profiles on Figure 4 but
446 still captures the deep layers of moist air in the upper troposphere between 261 and 147 hPa. To facilitate the comparison of
447 CFH and MLS water vapor profiles in the upper troposphere and stratosphere where water vapor mixing ratios decrease by 3
448 orders of magnitude, we compute a mean percent difference of the MLS collocated profiles to the CFH and MLS data (i.e.,
449 percent difference = $(\text{MLS} - \text{CFH}) / ((\text{CFH} + \text{MLS}) / 2) \times 100$). The same definition is used in Davis et al. (2016) and ensures that
450 the distribution of percent difference at each pressure level is not skewed toward positive values larger than 100% (since water
451 vapor values are constrained to be positive). In addition, this facilitates comparison with the study of Davis et al. (2016) that
452 established a comparison between the 2004-2015 MLS water vapor data record and both routine monitoring and field campaign
453 frost point hygrometer balloon soundings at various stations around the world.

454 Several factors could explain why a dry bias exists between the mean MLS profile and CFH convolved profile on 3 March
455 2017. First, the 3-km deep wet layer observed on March 2017 in the CFH profile will not be well captured by MLS with a 2-
456 3 km vertical resolution in the upper troposphere. In addition, the CFH launch on 3 March 2017 at 18 UTC was planned using
457 FLEXPART Lagrangian trajectory analysis and satellite images in the days prior to the launch to sample the convective
458 detrainment of TC Enawo. Therefore, the planning of the CFH launch on 3 March 2017 was optimal to sample moist air from
459 convective detrainment and an average of 3 MLS coincident profiles over a larger region/time window could be an
460 underestimate of the storm related moistening. It is also known that the stirring of air masses due to tropical cyclones generates
461 a rather inhomogeneous atmospheric composition up to the TTL (Cairo et al., 2008 and references therein). It is possible that
462 the CFH on 3 March 2017 sampled a fresher tropospheric filament with higher humidity than the 3 MLS profiles.

463

464 On 25 January 2016, the mean MLS water vapor profile agrees well with the convolved CFH profile over the entire lower
465 tropical stratosphere within layer L3. The mean percent difference is $+7 \pm 10\%$ ($+0.3$ ppmv) and lies within the previously
466 published uncertainty of both instrument (Hurst et al., 2014; Vömel et al., 2007a; Davis et al., 2016; Yan et al., 2016).

467 On 3 March 2017, larger differences of +18% (~0.6 ppmv) are observed in the lower stratosphere, between 121 and 32 hPa. It
468 is not clear why there are larger differences in the stratosphere on 3 March 2017. Both CFH instruments launched on 25 January
469 25 2016 and 3 March 2017 were prepared by the same operator and calibrated using the same recommended procedure. During
470 these two flights, the CFH data streams were transmitted to receiving equipment on the ground through the Internet
471 radiosonde. From an instrumental standpoint, there is nothing that might explain a CFH dry bias on 3 March 2017 compared
472 to 25 January 2016. Unfortunately, the CFH sondes are not recovered on the island after each flight as they land in the ocean
473 and thus it was not possible to examine in more details the instrument after the flight on 3 March 2017. To our knowledge, the
474 CFH instrument on that night has measured as well as it could in the stratosphere. Even though the CFH instrument launched
475 on 3 March 2017 had a dry bias of 1 ppmv in the stratosphere, such bias does not affect the results of this paper found for TC
476 Enawo.

477 Overall, the MLS mean profile agrees within uncertainty range with the CFH profile on 25 January 2016. On 3 March 2017,
478 the MLS mean profile is drier than CFH in the upper troposphere, probably due to a lack of vertical resolution in MLS, and
479 inhomogeneity in the atmospheric composition.

480 **5.2 Temperature anomaly**

481 The hypothesis of a potential influence of convection on the CFH water vapor profile is further tested by analysing the profile
482 of temperature anomaly. A seasonal mean (December-March) temperature profile is computed for the period 1997-2017 using
483 the NDACC/SHADOZ dataset. The weekly NDACC/SHADOZ launch is performed at the airport in the north part of the island
484 (Gillot, 20 m a.s.l.). The flying distance between the Maïdo Observatory and the airport is ~20 km so while boundary layer
485 temperature values will differ for the two sites, free troposphere/TTL temperature distributions can be compared as they are
486 less influenced by topography. The seasonal mean CPT height is 17.31 km for the period December-March with a mean CPT
487 temperature of 193.90 K (Table 1). The tropical tropopause is higher and colder during austral summer as a response to large-
488 scale upwelling in the tropical stratosphere (Yulaeva et al., 1994) and convection (Highwood and Hoskins 1998). The iMet
489 radiosonde temperature profiles are then compared to the seasonal mean NDACC/SHADOZ temperature profile. The upper
490 panels on Figure 5 show temperature profiles from NDACC/SHADOZ and the iMet radiosonde. The black line shows the
491 NDACC/SHADOZ seasonal mean temperature profile while the red line corresponds to the iMet temperature profile observed
492 at the Maïdo Observatory.

493 A large positive temperature anomaly is observed on 25 January 2016 over a broad tropospheric region from 2 to 16 km (mean
494 amplitude of +2.5 K) with a peak warming of +4.6 K at 10km (Figure 5, magenta line). On 3 March 2017, a warm temperature
495 anomaly is mostly observed between 6 and 14 km (mean amplitude of +1.1 K) with a peak value of +3.1 K near 12 km. The

496 stronger warming of the troposphere observed in January 2016 may be due to the strong 2015/2016 El Niño. The connection
497 between interannual variations in tropical tropospheric temperature and ENSO is well established (e.g., Yulaeva and Wallace
498 1994; Soden 2000). Using 13-year of temperature data from the tropospheric channel of the microwave sounding unit (MSU-
499 2), Yulaeva and Wallace (1994) showed that a tropospheric warming occurs almost uniformly over the tropics and that the
500 magnitude of the warming is around 0.5-1°C for strong El Niño years. Chiang and Sobel (2002) updated the analysis of Yulaeva
501 and Wallace to include the response to the strong 1997/98 El Niño (ONI of +2.2 K in DJF 1998) and indicated MSU-2
502 temperature anomaly of ~1.2 K in January 1998 (cf. Figure 1 of Chiang and Sobel, 2002). Note that the MSU-2 temperature
503 data used in these studies provide a measure of the mean temperature of the 1000-200 mb layer (corresponding to the surface
504 to ~ 11 km using a scale height of 7 km). Thus, part of the strong tropospheric warming (especially in the lower part of the
505 troposphere) observed in January 2016 may be due to the strong 2015/2016 El Niño (ONI of +2.5 K in DJF 2016). Assuming
506 a tropospheric warming of ~ 1K in response to a strong El Niño, the magnitude of the upper tropospheric warming observed
507 on 25 January 2016 (mean amplitude of 3.4 K between 10 and 14 km) becomes more similar to the one observed on 3 March
508 2017 (mean amplitude of 1.9 K between 10 and 14 km) if the effect of the 2015/2016 El Niño is removed.

509 Figure 5 indicates cold temperature anomalies within 16-19 km above the tropospheric warm anomalies on 25 January 2016.
510 The mean amplitude of the 16-19 km temperature anomaly is -1.6 K with a maximum cooling of -3.6 K at 18 km. A similar
511 feature is observed on 3 March 2017, with a cooling between 14 and 17 km with a mean amplitude of -2 K and maximum
512 cooling of -4.5 K at 15.1 km. The upper tropospheric warming and near tropopause cooling observed on both dates is consistent
513 with a temperature response to deep convection (e.g. Sherwood et al., 2003; Holloway and Neelin, 2007; Paulik and Birner,
514 2012). The cooling around the tropopause can be explained by either radiative cooling by cirrus clouds over the regions of
515 deep convection (Hartmann et al., 2001) or diabatic cooling through convective detrainment (Sherwood et al., 2003; Kuang
516 and Bretherton, 2004). CPT properties can also be modified by convectively driven waves (Zhou and Holton, 2002; Randel et
517 al., 2003).

518 Paulik and Birner (2012) investigated the deep convective temperature signal based on SHADOZ ozone and temperature data.
519 Low ozone concentrations in the upper troposphere are indicative of convective transport from the boundary layer. They looked
520 at temperature anomalies corresponding to low ozone anomalies between 12 and 18 km, thus temperature anomalies influenced
521 by deep convection. A strong warming was observed near the level of main convective outflow at ~12 km and cooling was
522 more pronounced above ~ 15 km and near the CPT at ~17 km. Thus, the upper tropospheric warm temperature anomalies as
523 well as cold temperature above 15 km and near the tropopause on Figure 5 are coherent with a deep convective temperature
524 signal. Paulik and Birner's study also showed that the amplitude of the temperature anomalies increases as convection
525 strengthens with a warming of ~2K in the upper troposphere and a cooling of around -3K near 16 km (cf. Figure 5 of Paulik
526 and Birner, 2012). Using CloudSat observations of deep convective clouds and COSMIC GPS temperature profiles, they

527 showed that the deep convective temperature signal (i.e. anomalously warm upper troposphere and an anomalously cold upper
528 TTL) was only present for deep convective clouds above 15 km. Although the magnitude of the temperature anomalies
529 decreases with increasing distance from convection, they observed a deep convective temperature signal during DJF ~3500
530 km away from the convective event. Within 1000 km of the deepest convection (deep convective clouds above 17 km), the
531 convective temperature anomaly exceeds 0.75 K in the upper troposphere and ranges from -1 K to -2.0 K near 16 km. In our
532 case, the deepest convective clouds with cloud tops colder than 190 K are 1000 km away from the island on 22-25 January
533 2016 and are closer from the island at ~500 km on 28 February-3 March 2017 (Figure 2). Although deep convective clouds
534 observed on 22-25 January 2016 and 28 February-3 March 2017 were not in the immediate vicinity, relatively fast-moving
535 gravity waves caused by deep convection could spread the deep convective temperature signals over large regions in short
536 amounts of time (Holloway and Neelin, 2007). The temperature anomalies in Figure 5 are much larger than those reported by
537 Paulik and Birner for temperature profiles around the time (± 6 hours) and location of deep convection (within 1000 km).
538 However, we are studying deep convective temperature anomalies associated with two individual events while their deep
539 convective temperature signal was estimated using 4 years of COSMIC data. Therefore, their estimates correspond to an
540 average deep convective temperature signal; such a signal is likely larger when considering larger/more organized convective
541 events such as tropical storms.

542 Hence, the temperature anomalies derived from the 25 January 2016 and 3 March 2017 profiles are coherent with a deep
543 convective outflow in the upper troposphere.

544 **5.3 Water vapor anomaly**

545 To further assess the impact of TS Coentim and TC Enawo on the UTLS water vapor content, we compare the convolved CFH
546 profiles to a monthly climatological MLS water vapor profile as there are no long-term stratospheric water vapor measurements
547 at Réunion Island. For each year between 2004 and 2017, MLS water vapor profiles within $\pm 5^\circ$ latitude and $\pm 10^\circ$ longitude of
548 Réunion Island and over a period of 15 days surrounding the launch date, i.e. 10 January-9 February for 25 January 2016 and
549 16 February-18 March 18 for 3 March 2017, are used to define a monthly climatological water vapor profile. We also computed
550 a non-convective monthly climatological MLS water vapor profile by excluding MLS water vapor profiles with coincident
551 low upper-tropospheric ozone (probably affected by convection, Paulik and Birner [2012]). The non-convective and monthly
552 climatological MLS water vapor profile (using all profiles) look very similar (not shown). Thus, the climatological MLS water
553 profile using all profiles is used for comparison with the water vapor measurements on 25 January 2016 and 3 March 2017.

554 The monthly climatological MLS water vapor profiles and CFH convolved profiles are shown on Figure 9. Both monthly
555 climatological water vapor profiles have comparable minimum water vapor mixing ratio at 83 hPa (3.5 ± 0.6 ppmv and $3.3 \pm$

556 0.5 ppmv for the January and March climatologies respectively). In the upper troposphere (316-178 hPa) the climatologies
557 have mean values of 277.6 ± 269.2 ppmv and 266.1 ± 253.2 ppmv for January and March respectively. High variability in the
558 UT is consistent with deep convection being more active during austral summer. Higher UT water vapor content in January
559 relative to March is in agreement with the fact that the austral summer season reaches its peak in January/February. Both
560 January and March climatologies have comparable TTL (147-68 hPa) water vapor content (5.3 ± 1.8 ppmv and 5.1 ± 1.7 ppmv
561 for January and March respectively). The climatological mean stratospheric (56-22 hPa) value is 4.2 ± 1.3 ppmv for both
562 months.

563 Relative water vapor differences are defined with respect to the monthly climatological profile (i.e., relative difference = (CFH
564 - MLS Climatology)/MLS Climatology x100) and are displayed on the bottom panels of Figure 9. In addition to the CFH
565 convolved profile, we also compared the mean of MLS coincident profiles to the MLS monthly climatological profile for 25
566 January 2016 and 3 March 2017.

567 On 25 January 2016, the mean of MLS coincident profiles and the CFH convolved profile show a peak of $\sim 30\%$ or 7.7ppmv
568 in the relative difference with the MLS climatology in layer L1, but the pressure level of this peak differs in the two profiles
569 with a peak at 178 hPa for the CFH convolved profile and 147 hPa for the mean of coincident MLS profiles.

570 To further evaluate the portion of the profiles that were influenced by convection, we calculated a convective fraction profile.
571 For each pressure level depicted on Figure 9, 50,000 FLEXPART backtrajectories were initialized. A backtrajectory was
572 tagged as convectively influenced when the IR BT observed by METEOSAT 7 falls below 230 K over the previous 7 days,
573 and if the altitude of the backtrajectory falls below 5 km, indicating a lower tropospheric origin. Hence, the convective fraction
574 profile represents the percentage of trajectories for each pressure level that were considered as convective following those
575 criterias. The convective fraction profile reaches a maximum of 60% at 147hPa, and confirms that layer L1 and the bottom
576 part of layer L2 are convective. The FLEXPART backtrajectories from figure 6 and the values of the convective fraction
577 profile confirm that the positive water vapor anomalies observed in layer L1 are associated with the convective outflow of TS
578 Corentin.

579 On 3 March 2017, the hydration of the upper troposphere in layer L4 (between 215 and 121 hPa) is much more pronounced in
580 the CFH convolved profile with a peak of value of $\sim 180\%$ or 45ppmv at 178 hPa. For the mean of MLS coincident profiles,
581 the moistening is not as large with a relative difference of 36% or 8.7ppmv at 178 hPa. The convective fraction profile had
582 values of 60% at 178 and 147hPa, confirming that layer L4 were influenced by convection.

583 Ray and Rosenlof (2007) used measurements from AIRS to assess the impact of tropical cyclones in the Atlantic and Pacific
584 basins on the amount of water vapor in the tropical UT. They showed that tropical cyclones can hydrate a deep layer of the

585 surrounding upper troposphere by ~30-50 ppmv or more within 500 km of the eye compared to the surrounding average water
586 vapor mixing ratios (cf. Figure 3 of Ray and Rosenlof, 2007). They also looked at the evolution of UT water vapor changes as
587 a function of the storm intensity as measured by the peak wind speed (cf. Figure 5 of Ray and Rosenlof, 2007). In both the
588 Atlantic and western Pacific basins, the average water vapor at 223 hPa around the storm center steadily increased from 4 to 5
589 days prior to peak cyclone intensity to 2 days following peak cyclone intensity. The average water vapor enhancement in the
590 two ocean basins was from 5 to 20 ppmv with an increase as high as 30-40 ppmv for some cyclones in the western Pacific.
591 The CFH launch on 3 March 2017 18 UTC occurred 3.5 days before Enawo reached its peak intensity on 7 March at 06 UTC
592 (pressure at the center of 932 hPa, ten-minute maximum sustained winds of 204 km hr⁻¹) and the storm center was ~ 700 km
593 away from the island. Thus, deep convection associated with TC Enawo may have caused the strong increase in UT water
594 vapor observed on 3 March 2017. Ongoing work with MLS data to apply the methodology of Ray and Rosenlof (2007) to
595 assess hydration of the UTLS by tropical cyclones for the 2004-2017 cyclone seasons in the southwest Indian Ocean is under
596 way. This will be the focus of a future study but preliminary results indicate water vapor differences of 35% to 48% at between
597 178 and 261 hPa for categories 2 to 4 hurricanes on the Saffir-Simpson scale. Ray and Rosenlof (2007) indicated that tropical
598 cyclones hydrate a deep layer of the UT in the vicinity of the cyclones by up to 50% above monthly mean water vapor mixing
599 ratios. Therefore, our estimate of UT water vapor increases of 20 to 100% using CFH&MLS data for TS Corentin (Category
600 1 hurricane at its peak intensity) and TC Enawo (Category 4 hurricane at its peak intensity) are in broad agreement with our
601 estimates based on the 2004-2017 MLS data and the study of Ray and Rosenlof (2007).

602 At 100 hPa (within layer L2), both MLS and CFH data are 20% (-0.7ppmv) below the climatological monthly mean values on
603 25 January 2016. This would be coherent with the near tropopause cooling observed on Figure 5 and the presence of deep
604 convection around Réunion Island. In addition, TTL cirrus clouds were observed north of the island on both dates (Figure 5).
605 Convectively generated or in-situ cirrus clouds in the TTL can dehydrate the tropopause region. Jensen et al. (1996) showed
606 that ice clouds formed by large-scale vertical motions can result in depletion of water vapor mixing ratio by about 0.4 ppmv.
607 Chae et al. (2011) investigated temperature and water vapor changes due to clouds in the TTL using MLS, CALIPSO and
608 CloudSat datasets. They noted that generally clouds humidify the environment near 16 km (~100 hPa) or lower but dehydrate
609 the TTL above 16 km.

610 On 25 January 2016, CFH and MLS data are 11% (+0.4 ppmv) and 18% (+0.7 ppmv) moister than the climatological values
611 at 68 hPa (within layer L3), above the tropopause. Observational and modeling studies have indicated that overshooting
612 convection can moisten the lower stratosphere by injecting water vapor or ice crystals directly above the overshooting clouds
613 (e.g. Danielsen, 1993; Corti et al., 2008; Dauhut et al., 2015; Frey et al., 2015; Allison et al., 2018). In our case, the observation
614 on 25 January 2016 was not made close to the deepest convective clouds that were ~1000 km north of the island (Figure 2),
615 but was downwind of TS Corentin, as shown by the FLEXPART analysis (Figure 6). However, FLEXPART backtrajectories

616 indicate that the air masses at 68h Pa (layer L3) originate from the South East Indian Ocean in the 20°S-30°S latitude band
617 where the MLS water vapor anomaly for January 2016 is around 0.5 ppmv most likely due to the impact of the 2016 strong El
618 Niño event. Hence, the positive anomaly against the climatological value can also be explained by horizontal advection from
619 the South East Indian Ocean toward Reunion island.

620 It is difficult to conclude whether TC Enawo had a direct impact on water vapor in the lower stratosphere by using only the
621 CFH observation on 3 March 2017. The FLEXPART analysis indicated that the CFH sounding did not sample the lower
622 stratosphere downwind of Enawo.

623 Ongoing work with the mesoscale model Meso-NH at a 2-km resolution for TC Enawo for the period 2-7 March 2017 indicates
624 that deep convective clouds within 500 km of the cyclone eye can inject ice crystals and moisten the lower stratosphere,
625 resulting in an average anomaly of ~2ppmv within 500 km of the tropical cyclone eye. The strongest humidification in the
626 lower stratosphere (17-19 km; ~88-66 hPa) was found after March 4 when the storm stalled over the ocean (while intensifying)
627 and after March 6 when it reached its peak intensity. Thus, the CFH observation on 3 March 2017 was made before TC Enawo
628 had influenced the lower stratosphere above 100 hPa. This is further confirmed by the fact CALIOP did not have a lower
629 stratospheric signal on Figure 6.

630 Tropical cyclones are unique among tropical convective systems in that they persist for many days and thus could affect the
631 UTLS more than other mesoscale convective systems. Clouds in tropical cyclones often reach to and sometimes beyond the
632 tropopause (e.g., Romps and Kuang 2009). Allison et al. (2018) have investigated the vertical transport of water vapor by the
633 2013 tropical cyclone Ingrid in the North Atlantic. Results of their high-resolution numerical simulations indicated that
634 hydration occurred between 17.5 and 21 km (83 to 56 hPa) due to the injection of ice crystals. As the exact role of deep
635 convection, and tropical cyclones in particular, in hydrating the lower stratosphere is still under debate, additional TTL
636 observations of water vapor and modeling work are needed to quantify the overall impact of convection on TTL and LS water
637 vapor. High-resolution (2 km) numerical simulations of TC Enawo for the period 2-7 March 2017 are underway to gain a
638 closer look at the effect of TC convection on TTL temperature and water vapor. This work will be the subject of a subsequent
639 study.

640 **7 Summary**

641 Two balloon launches from the Mado Observatory were specifically planned using the FLEXPART Lagrangian model and
642 METEOSAT 7 infrared images to sample the convective outflow from Tropical Storm Corentin on 25 January 2016 and
643 Tropical Cyclone Enawo on 3 March 2017. Balloon-borne measurements of CFH water vapor, ozone and iMET temperature
644 and water vapor lidar measurements, showed that both storms humidified the TTL, with RH_{ice} values exceeding 50% for TS

645 Corentin and 90% for TC Enawo in the upper troposphere. Comparing the two CFH profiles to the climatological monthly
646 mean MLS water vapor profiles, positive anomalies of water vapor were identified with peak values of 7.7 ppmv for TS
647 Corentin and 45 ppmv for TC Enawo at 17hPa. According to the FLEXPART backtrajectories and METEOSAT 7 infrared
648 images, those air masses originated from convectively active regions of TS Corentin and TC Enawo and were lifted from the
649 lower troposphere to the upper troposphere around one day before the planned balloon launches. In addition, the CALIOP
650 satellite measurements indicated cirrus clouds north of Réunion Island for the same altitude range for both storms.

651 According to the CFH profile on 25 January 2016 and MLS climatology, air masses measured near the tropopause were
652 anomalously dry around 100 hPa and anomalously wet around 68 hPa in the lower stratosphere. FLEXPART backtrajectories
653 were used to find the origin of these layers that could be traced back to TS Corentin upper-tropospheric divergent flow and
654 active convective regions. Deep convective clouds and cirrus clouds may have dehydrated the region around 100hPa.
655 According to FLEXPART backtrajectories, the positive anomaly at 68hPa can be explained by a horizontal transport from the
656 South East Indian Ocean. The South East Indian Ocean had a positive water vapor anomaly of ~0.5ppmv in January 2016 most
657 likely due to the strong 2016 El Niño event (Avery et al., 2017).

658 On the contrary, no water vapor anomaly was found near or above the tropopause on 3 March 2017 as the tropopause region
659 was not downwind of TC Enawo. According to FLEXPART backtrajectories, those air masses stayed away from the upper-
660 tropospheric dynamics of TC Enawo and its convective active regions. Hence the tropopause region on 3 March 2017 was not
661 affected by Enawo, at least not at the time of the balloon launch and at this stage of Enawo's development.

662 This study showed the impact of two tropical cyclones on the humidification of the TTL. It also demonstrates the need to
663 develop balloon borne high precision observations in regions where TTL in-situ observations are sparse, such as the tropics
664 and the SWIO in particular. High-resolution accurate observations of water vapor are needed to document the impact of tropical
665 cyclones and deep convection in general on the TTL. The impact of tropical cyclones on the TTL water vapor budget will be
666 analyzed in a more quantitative way using MLS data and tropical cyclones best tracks from 2004 to 2017 in a subsequent
667 paper. In addition, the impact of deep convection and overshooting clouds within TC Enawo on the water vapor budget of the
668 TTL will be analyzed using high-resolution (2 km) mesoscale simulation of TC Enawo.

669 *Data availability.* MLS water vapor data used in this study are available at <https://mls.jpl.nasa.gov/> and CALIPSO L1B lidar
670 data are available at https://eosweb.larc.nasa.gov/project/calipso/lidar_l1b_profile_table. The NDACC/SHADOZ ozone
671 measurements for Réunion Island are available at <https://tropo.gsfc.nasa.gov/shadoz/Reunion.html>. The SWOOSH dataset is
672 available at <https://data.nodc.noaa.gov/cgi-bin/iso?id=gov.noaa.ncdc:C00958>. The CFH and lidar water vapor data are
673 available from the authors (SE, VD, PK) upon request. The FLEXPART Lagrangian trajectories can be requested from the

674 corresponding author Stephanie Evan (stephanie.evan@univ-reunion.fr).

675

676 *Author contributions.* All authors contributed to the paper. SE wrote the manuscript with contributions from JB, KR, SD, DH,
677 FP, JMM, VD, GP, HV, PK, JPC. SE, JB, FP, JMM, DH, JPC, VD, GP and HV performed the CFH/Ozone/Lidar
678 measurements. HV processed the CFH data. SE and JB performed the FLEXPART simulations. SM provided the SWOOSH
679 dataset. All authors revised the manuscript draft.

680 *Competing interests.* The authors declare that they have no conflict of interest.

681 *Acknowledgments*

682 We thank the Aura Science Team for the MLS data (<https://mls.jpl.nasa.gov/>) and the CALIPSO science team for the L1B
683 lidar data (https://eosweb.larc.nasa.gov/project/calipso/lidar_l1b_profile_table).

684 OPAR (Observatoire de Physique de l'Atmosphère à La Réunion, including Maïdo Observatory) is part of OSU-R
685 (Observatoire des Sciences de l'Univers à La Réunion) which is being funded by Université de la Réunion, CNRS-INSU,
686 Météo-France, and the french research infrastructure ACTRIS-France (Aerosols, Clouds and Trace gases Research
687 Infrastructure). OPAR's water vapor lidar and ozone radiosounding belong to the international network NDACC (Network for
688 the Detection of Atmospheric Composition Change). This work was supported by the French LEFE CNRS-INSU Program
689 (VAPEURDO).

690 S. Evan thanks Susanne Koerner (DWD/GRUAN Leadcentre, Germany) for her training on the CFH instrument.

691 **References**

692 Allison, T., Fuelberg, H., and Heath, N.: Simulations of vertical water vapor transport for TC Ingrid (2013), *J. Geophys. Res.*,
693 123, 8255-8282, <https://doi.org/10.1029/2018JD028334>, 2018.

694 Avery, M. A., Davis, S. M., Rosenlof, K. H., Ye, H., and Dessler, A.: Large anomalies in lower stratospheric water vapor and
695 ice during the 2015-2016 El Niño, *Nat. Geosci.*, 10, 405-409. <https://doi.org/10.1038/ngeo2961>, 2017.

696 Baldwin, M. P., Gray, L. J., Dunkerton, T. J., Hamilton, K., Haynes, P. H., Holton, J. R., Alexander, M. J., Hirota, I.,
697 Horinouchi, T., Jones, D. B. A., Marquardt, C., Sato, K., and Takahashi, M.: The quasi-biennial oscillation, *Rev. Geophys.*,

698 <https://doi.org/10.1029/1999RG000073>, 2001

699 Baray J.-L., Y. Courcoux, P. Keckhut, T. Portafaix, P. Tulet, J.-P. Cammas, A. Hauchecorne, S. Godin-Beekmann, M. De
700 Mazière, C. Hermans, F. Desmet, K. Sellegri, A. Colomb, M. Ramonet, J. Sciare, C. Vuillemin, C. Hoareau, D. Dionisi, V.
701 Dufлот, H. Vèrèmes, J. Porteneuve, F. Gabarrot, T. Gaudo, J.-M. Metzger, G. Payen, J. Leclair de Bellevue, C. Barthe, F.
702 Posny, P. Ricaud, A. Abchiche, and R. Delmas, Maïdo observatory: a new high-altitude station facility at Reunion Island (21°
703 S, 55°E) for long-term atmospheric remote sensing and in situ measurements, *Atmos. Meas. Tech.*, 6, 2865-2877, 2013

704 Bechtold, P., Köhler, M., Jung, T., Doblas-Reyes, F., Leutbecher, M., Rodwell, M. J., Vitart, F. and Balsamo, G., Advances
705 in simulating atmospheric variability with the ECMWF model: From synoptic to decadal time-scales., *Q. J. Roy. Meteorol.*
706 *Soc* 134: 1337-1351, <https://doi.org/10.1002/qj.289>, 2008.

707 Bechtold, P., Semane, N., Lopez, P., Chaboureau, J.-P., Beljaars, A., and Bormann, N., Representing Equilibrium and
708 Nonequilibrium Convection in Large-Scale Models, *J. Atmos. Sci.*, 71, 734–753, <https://doi.org/10.1175/JAS-D-13-0163.1>,
709 2014.

710 Bodeker, G. E., Bojinski, S., Cimini, D., Dirksen, R. J., Haeffelin, M., Hannigan, J. W., Hurst, D., Madonna, F., Maturilli, M.,
711 Mikalsen, A. C., Philipona, R., Reale, T., Seidel, D. J., Tan, D. G. H., Thorne, P. W., Vömel, H., and Wang, J.: Reference
712 upper-air observations for climate: From concept to reality, *B. Am. Meteorol. Soc.*, 97, 123–135,
713 <https://doi.org/10.1175/BAMS-D-14-00072.1>, 2015.

714 Bovalo, C., C. Barthe, and N. Bègue, A lightning climatology of the South West Indian Ocean, *Nat. Hazards Earth Syst. Sci.*,
715 12, 2659–2670, <https://doi.org/10.5194/nhess-12-2659-2012>, 2012.

716 Brunamonti, S., Jorge, T., Oelsner, P., Hanumanthu, S., Singh, B. B., Kumar, K. R., Sonbawne, S., Meier, S., Singh, D.,
717 Wienhold, F. G., Luo, B. P., Boettcher, M., Poltera, Y., Jauhiainen, H., Kayastha, R., Karmacharya, J., Dirksen, R., Naja, M.,
718 Rex, M., Fadnavis, S., and Peter, T.: Balloon-borne measurements of temperature, water vapor, ozone and aerosol backscatter
719 on the southern slopes of the Himalayas during StratoClim 2016–2017, *Atmos. Chem. Phys.*, 18, 15937–15957,
720 <https://doi.org/10.5194/acp-18-15937-2018>, 2018.

721 Cairo, F., Buontempo, C., MacKenzie, A. R., Schiller, C., Volk, C. M., Adriani, A., Mitev, V., Matthey, R., Di Donfrancesco,
722 G., Oulanovsky, A., Ravegnani, F., Yushkov, V., Snels, M., Cagnazzo, C., and Stefanutti, L.: Morphology of the tropopause
723 layer and lower stratosphere above a tropical cyclone: a case study on cyclone Davina (1999), *Atmos. Chem. Phys.*, 8, 3411–
724 3426, <https://doi.org/10.5194/acp-8-3411-5-2008>, 2008.

725 Chae, J. H., Wu, D. L., Read, W. G., and Sherwood, S. C.: The role of tropical deep convective clouds on temperature, water
726 vapor, and dehydration in the tropical tropopause layer (TTL), *Atmos. Chem. Phys.*, 11, 3811–3821,
727 <https://doi.org/10.5194/acp-11-3811-2011>, 2011.

728 Chiang, J.C. and A.H. Sobel, Tropical Tropospheric Temperature Variations Caused by ENSO and Their Influence on the
729 Remote Tropical Climate. *J. Climate*, 15, 2616–2631, [https://doi.org/10.1175/1520-0442\(2002\)015<2616:TTTVCB>2.0.CO;2](https://doi.org/10.1175/1520-0442(2002)015<2616:TTTVCB>2.0.CO;2), 2012

731 Corti, T., Luo, B. P., de Reus, M., Brunner, D., Cairo, F., Mahoney, M. J., Martucci, G., Matthey, R., Mitev, V., dos Santos,
732 F. H., Schiller, C., Shur, G., Sitnikov, N. M., Spelten, N., Vössing, H. J., Borrmann, S., and Peter, T.: Unprecedented evidence
733 for deep convection hydrating the tropical stratosphere, *Geophys. Res. Lett.*, 35, L10810,
734 <https://doi.org/10.1029/2008GL033641>, 2008.

735 Danielsen, E. F.: A dehydration mechanism for the stratosphere, *Geophys. Res. Lett.*, 9, 605–608, 1982.

736 Dauhut, T., Chaboureaud, J. P., Escobar, J., and Mascart, P.: Large-eddy simulations of the convective making the
737 stratosphere wetter, *Atmos. Sci. Lett.*, 16, 135–140, <https://doi.org/10.1002/asl2.534>, 2015.

738 Davis, S. M., Rosenlof, K. H., Hassler, B., Hurst, D. F., Read, W. G., Vömel, H., Selkirk, H., Fujiwara, M., and Damadeo, R.:
739 The Stratospheric Water and Ozone Satellite Homogenized (SWOOSH) database: a long-term database for climate studies,
740 *Earth Syst. Sci. Data*, 8, 461–490, <https://doi.org/10.5194/essd-8-461-2016>, 2016.

741 Davis, S. M., Liang, C. K., and Rosenlof, K. H.: Interannual variability of tropical tropopause layer clouds, *Geophys. Res.
742 Lett.*, 40, 2862–2866. <https://doi.org/10.1002/grl.50512>, 2013.

743 Dessler, A. E. and Sherwood, S. C.: A model of HDO in the tropical tropopause layer, *Atmos. Chem. Phys.*, 3, 2173–2181,
744 <https://doi.org/10.5194/acp-3-2173-2003>, 2003.

745 Emanuel, K. A., and Zivkovic-Rothman, M.: Development and evaluation of a convection scheme for use in climate
746 models, *J. Atmos. Sci.*, 56, 1766–1782, 1999.

747 Folkins, I. and R.V. Martin: The Vertical Structure of Tropical Convection and Its Impact on the Budgets of Water Vapor and
748 Ozone. *J. Atmos. Sci.*, 62, 1560–1573, <https://doi.org/10.1175/JAS3407.1>, 2005.

749 Frey, W., Schofield, R., Hoor, P., Kunkel, D., Ravegnani, F., Ulanovsky, A., Viciani, S., D'Amato, F., and Lane, T. P.: The

750 impact of overshooting deep convection on local transport and mixing in the tropical upper troposphere/lower stratosphere
751 (UTLS), *Atmos. Chem. Phys.*, 15, 6467–6486, <https://doi.org/10.5194/acp-15-6467-2015>, 2015.

752 Fueglistaler, S., Dessler, A. E., Dunkerton, T. J., Folkins, I., Fu, Q., and Mote, P. W.: Tropical tropopause layer, *Rev. Geophys.*,
753 47, RG1004, <https://doi.org/10.1029/2008RG000267>, 2009.

754 Goff, J. A. and Gratch, S., Low-pressure properties of water from –160 to 212 F. *Trans. Am. Soc. Heating Air-Cond. Eng.*,
755 52, 95–122 (presented at the 52nd annual meeting of the American society of heating and ventilating engineers, New York),
756 1946.

757 Hartmann, D.L, Holton J.R. and Q. Fu, The heat balance of the tropical tropopause, cirrus, and stratospheric dehydration.
758 *Geophys. Res. Lett.*, 28, <https://doi:10.1029/2000GL012833>, 2001.

759 Highwood, E. J. and Hoskins, B. J.: The tropical tropopause, *Q. J. Roy. Meteorol. Soc.*, 124, 1579-1604,
760 <https://doi.org/10.1002/qj.49712454911>, 1998.

761 Ho C-H, Kim J-H, Jeong J-H, Kim H-S, and Chen D.: Variation of tropical cyclone activity in the South Indian Ocean: El
762 Niño-Southern Oscillation and Madden-Julian Oscillation effects. *J. Geophys. Res.*, 111: D22101,
763 <https://doi:10.1029/2006JD007289>, 2006

764 Holloway, C.E, and J.D. Neelin: The convective cold top and quasi equilibrium. *J. Atmos. Sci.* 64, 1467–
765 1487.doi:10.1175/JAS3907.1, 2007.

766 Holton, J. R., and A. Gettelman: Horizontal transport and the dehydration of the stratosphere. *Geophys. Res. Lett.*, 28, 2799–
767 2802, <https://doi.org/10.1029/2001GL013148>, 2001.

768
769 Hurst, D. F., Hall, E. G., Jordan, A. F., Miloshevich, L. M., Whiteman, D. N., Leblanc, T., Walsh, D., Vömel, H., and
770 Oltmans, S. J.: Comparisons of temperature, pressure and humidity measurements by balloon-borne radiosondes and frost
771 point hygrometers during MOHAVE-2009, *Atmos. Meas. Tech.*, 4, 2777–2793, <https://doi.org/10.5194/amt-4-2777-2011>,
772 2011.

773 Hurst, D. F., Lambert, A., Read, W. G., Davis, S. M., Rosenlof, K. H., Hall, E. G., Jordan, A. F., and Oltmans, S. J.: Validation
774 of Aura Microwave Limb Sounder stratospheric water vapor measurements by the NOAA frost point hygrometer, *J. Geophys.*
775 *Res.-Atmos.*, 119, 1612–1625, doi:10.1002/2013jd020757, 2014

776 Jensen, E. J., O. B. Toon, H. B. Selkirk, J. D. Spinhirne, and Schoeberl M. R.: On the formation and persistence of subvisible
777 cirrus clouds near the tropical tropopause, *J. Geophys. Res.*, 101, 21,361–21,375, 1996.

778 Jensen, E. J., Ackerman, A. S., and Smith, J. A.: Can overshooting convection dehydrate the tropical tropopause layer?, *J.*
779 *Geophys. Res.-Atmos.*, 112, D11209, doi:10.1029/2006JD007943, 2007.

780 Jensen, E. J., Pfister, L., Jordan, D. E., Bui, T. V., Ueyama, R., Singh, H. B., Thornberry, T. D., Rollins, A. W., Gao, R., Fahey,
781 D. W., Rosenlof, K. H., Elkins, J. W., Diskin, G. S., DiGangi, J. P., Lawson, R. P., Woods, S., Atlas, E. L., Navarro Rodriguez,
782 M. A., Wofsy, S. C., Pittman, J., Bardeen, C. G., Toon, O. B., Kindel, B. C., Newman, P. A., McGill, M. J., Hlavka, D. L.,
783 Lait, L. R., Schoeberl, M. R., Bergman, J. W., Selkirk, H. B., Alexander, M. J., Kim, J.-E., Lim, B. H., Stutz, J., and Pfeilsticker,
784 K.: The NASA Airborne Tropical Tropopause Experiment: High-Altitude Aircraft Measurements in the Tropical Western
785 Pacific, *B. Am. Meteorol. Soc.*, 98, 129–143, <https://doi.org/10.1175/BAMS-D-14-00263.1>, 2017.

786 Jorge, T., Brunamonti, S., Poltera, Y., Wienhold, F. G., Luo, B. P., Oelsner, P., Hanumanthu, S., Sing, B. B., Körner, S.,
787 Dirksen, R., Naja, M., Fadnavis, S., and Peter, T.: Understanding cryogenic frost point hygrometer measurements after
788 contamination by mixed-phase clouds, *Atmos. Meas. Tech. Discuss.*, <https://doi.org/10.5194/amt-2020-176>, in review, 2020

789 Keckhut, P., Courcoux, Y., Baray, J.-L., Porteneuve, J., Vèrèmes, H., Hauchecorne, A., Dionisi, D., Posny, F., Cammas, J.-P.,
790 Payen, G., Gabarrot, F., Evan, S., Khaykin, S., Rüfenacht, R., Tschanz, B., Kämpfer, N., Ricaud, P., Abchiche, A., Leclairde-
791 Bellevue, J., and Dufлот, V.: Introduction to the Maïdo Lidar Calibration Campaign dedicated to the validation of upper air
792 meteorological parameters, *J. Appl. Remote Sens.*, 9, 094099, <https://doi.org/10.1117/1.JRS.9.094099>, 2015.

793 Khaykin, S. M., Engel, I., Vömel, H., Formanyuk, I. M., Kivi, R., Korshunov, L. I., Krämer, M., Lykov, A. D., Meier, S.,
794 Naebert, T., Pitts, M. C., Santee, M. L., Spelten, N., Wienhold, F. G., Yushkov, V. A., and Peter, T.: Arctic stratospheric
795 dehydration – Part 1: Unprecedented observation of vertical redistribution of water, *Atmos. Chem. Phys.*, 13, 11503–11517,
796 <https://doi.org/10.5194/acp-13-11503-2013>, 2013.

797 Kuang, Z., and C. S. Bretherton: Convective influence on the heat balance of the tropical tropopause layer: A cloud-resolving
798 model study, *J. Atmos. Sci.*, 61, 2919-2927, <https://doi.org/10.1175/JAS-3306.1>, 2004.

799 Lee, S.-K., Park, W., Baringer, M. O., Gordon, A. L., Huber, B., and Liu, Y.: Pacific origin of the abrupt increase in Indian
800 Ocean heat content during the warming hiatus, *Nat. Geosci.*, 8(6), 445-449, 2015.

801 Liu, C. and Zipser, E. J.: Global distribution of convection penetrating the tropical tropopause, *J. Geophys. Res.*, 110,
802 D23104, <https://doi.org/10.1029/2005JD006063>, 2005.

803 Magnusson, L., J.-R. Bidlot, M. Bonavita, A. R. Brown, P. A. Browne, G. De Chiara, M. Dahoui, S. T. K. Lang, T. McNally,
804 K. S. Mogensen, F. Pappenberger, F. Prates, F. Rabier, D. S. Richardson, F. Vitart, and S. Malardel: ECMWF Activities for

805 improved hurricane forecasts, <https://doi.org/10.1175/BAMS-D-18-0044.1>, 2018

806 Neumann, C.J.: "Global Overview" - Chapter 1" Global Guide to Tropical Cyclone Forecasting, WMO/TC-No. 560, Report
807 No. TCP-31, World Meteorological Organization; Geneva, Switzerland, 1993

808 Paulik, L. C. and Birner, T.: Quantifying the deep convective temperature signal within the tropical tropopause layer (TTL),
809 *Atmos. Chem. Phys.*, 12, 12183-12195, <https://doi.org/10.5194/acp-12-12183-2012>, 2012.

810 Randel, W. J., F. Wu, and W. Rivera Rios: Thermal variability of the tropical tropopause region derived from GPS/MET
811 observations, *J. Geophys. Res.*, 108(D1), 4024, <https://doi:10.1029/2002JD002595>, 2003

812 Ray, E. A., and Rosenlof, K. H.; Hydration of the upper troposphere by tropical cyclones, *J. Geophys. Res.*, 112, D12311,
813 <https://doi:10.1029/2006JD008009>, 2007.

814 Read, W. G., Lambert, A., Bacmeister, J., Cofield, R. E., Christensen, L. E., Cuddy, D. T., Daffer, W. H., Drouin, B. J., Fetzer,
815 E., Froidevaux, L., Fuller, R., Herman, R., Jarnot, R. F., Jiang, J. H., Jiang, Y. B., Kelly, K., Knosp, B. W., Kovalenko, L. J.,
816 Livesey, N. J., Liu, H. C., Manney, G. L., Pickett, H. M., Pumphrey, H. C., Rosenlof, K. H., Sabouchi, X., Santee, M. L.,
817 Schwartz, M. J., Snyder, W. V., Stek, P. C., Su, H., Takacs, L. L., Thurstans, R. P., Vomel, H., Wagner, P. A., Waters, J. W.,
818 Webster, C. R., Weinstock, E. M., and Wu, D. L.: Aura Microwave Limb Sounder upper tropospheric and lower stratospheric
819 H₂O and relative humidity with respect to ice validation, *J. Geophys. Res.-Atmos.*, 112, D24S35 doi:10.1029/2007JD008752,
820 2007.

821 Roca, R., M. Viollier, L. Picon, and Desbois M.: A multisatellite analysis of deep convection and its moist environment over
822 the Indian Ocean during the winter monsoon, *J. Geophys. Res.*, 107(D19), 8012, doi:10.1029/2000JD000040, 2002.

823 Romps, D. M., and Kuang, Z.: Overshooting convection in tropical cyclones, *Geophys. Res. Lett.*, 36, L09804,
824 <https://doi:10.1029/2009GL037396>, 2009

825 Schoeberl, M. R., Dessler, A. E., Wang, T., Avery, M. A., and Jensen, E. J.: Cloud formation, convection, and stratospheric
826 dehydration, *Earth and Space Science*, 1, 1-17, doi:10.1002/2014EA000014, 2014

827 Sherwood, S.C., Horinouchi, T., and Zeleznik, H.A.: Convective Impact on Temperatures Observed near the Tropical
828 Tropopause. *J. Atmos. Sci.*, 60, 1847–1856, [https://doi.org/10.1175/1520-0469\(2003\)060<1847:CIOTON>2.0.CO;2](https://doi.org/10.1175/1520-0469(2003)060<1847:CIOTON>2.0.CO;2), 2003

829 Stohl, A., Forster, C., Frank, A., Seibert, P., and Wotawa, G.: Technical note: The Lagrangian particle dispersion model

830 FLEXPART version 6.2, *Atmos. Chem. Phys.*, 5, 2461-2474, <https://doi.org/10.5194/acp-5-2461-2005>, 2005.

831 Soden, B.J.: The Sensitivity of the Tropical Hydrological Cycle to ENSO. *J. Climate*, 13, 538–549,
832 [https://doi.org/10.1175/1520-0442\(2000\)013<0538:TSOTTH>2.0.CO;2](https://doi.org/10.1175/1520-0442(2000)013<0538:TSOTTH>2.0.CO;2), 2000

833 Tao, C. and H. Jiang: Global Distribution of Hot Towers in Tropical Cyclones Based on 11-Yr TRMM Data. *J. Climate*, 26,
834 1371–1386, <https://doi.org/10.1175/JCLI-D-12-00291.1>, 2013.

835 Tian, E. W., Su, H., Tian, B., and Jiang, J. H. (2019). Interannual variations of water vapor in the tropical upper troposphere
836 and the lower and middle stratosphere and their connections to ENSO and QBO, *Atmospheric Chemistry and Physics*, 19,
837 9913-9926, doi:10.5194/acp-19-9913-2019.

838 Tiedtke, M.: A Comprehensive Mass Flux Scheme for Cumulus Parameterization in Large-Scale Models, *Mon. Weather Rev.*,
839 117, 1779–1800, [https://doi.org/10.1175/1520-0493\(1989\)117<1779:ACMFSF>2.0.CO;2](https://doi.org/10.1175/1520-0493(1989)117<1779:ACMFSF>2.0.CO;2), 1989

840 Tissier, A.-S. and Legras, B.: Convective sources of trajectories traversing the tropical tropopause layer, *Atmos. Chem. Phys.*,
841 16, 3383–3398, <https://doi.org/10.5194/acp-16-3383-2016>, 2016.

842 Thompson, A. M., Witte, J. C., McPeters, R. D., Oltmans, S. J., Schmidlin, F. J., Logan, J. A., Fujiwara, M., Kirchhoff, V. W.
843 J. H., Posny, F., Coetzee, G. J. R., Hoegger, B., Kawakami, S., Ogawa, T., Johnson, B. J., Vömel, H., and Labow, G.: Southern
844 Hemisphere Additional Ozonesondes (SHADOZ) 1998–2000 tropical ozone climatology 1. Comparison with Total Ozone
845 Mapping Spectrometer (TOMS) and ground-based measurements, *J. Geophys. Res.-Atmos.*, 108, 8238,
846 doi:10.1029/2001jd000967, 2003.

847 Toon, O. B., Starr, D. O., Jensen, E. J., Newman, P. A., Platnick, S., Schoeberl, M. R., Wennberg, P. O., Wofsy, S. C., Kurylo,
848 M. J., Maring, H., Jucks, K. W., Craig, M. S., Vasques, M. F., Pfister, L., Rosenlof, K. H., Selkirk, H. B., Colarco, P. R., Kawa,
849 S. R., Mace, G. G., Minnis, P., and Pickering, K. E.: Planning, implementation, and first results of the Tropical Composition,
850 Cloud and Climate Coupling Experiment (TC4), *J. Geophys. Res.*, 115, D00J04, <https://doi.org/10.1029/2009JD013073>, 2010.

851 Ueyama, R., Jensen, E. J., Pfister, L., and Kim, J.-E.: Dynamical, convective, and microphysical control on wintertime
852 distributions of water vapor and clouds in the tropical tropopause layer, *J. Geophys. Res.-Atmos.*, 120, 10483-10500,
853 <https://doi.org/10.1002/2015JD023318>, 2015.

854 Ueyama, R., Jensen, E. J., and Pfister, L.: Convective influence on the humidity and clouds in the tropical tropopause layer
855 during boreal summer. *J. Geophys. Res. Atmos.*, 123, 7576-7593, <https://doi.org/10.1029/2018JD028674>, 2018.

856 Vaughan, M., S. Young, D. Winker, K. Powell, A. Omar, Z. Liu, Y. Hu, and C. Hostetler: Fully automated analysis of space-
857 based lidar data: An overview of the CALIPSO retrieval algorithms and data products. *Proc. SPIE Int. Soc. Opt. Eng.*, 5575,
858 16-30, 2004.

859 Vèrèmes, H., Payen, G., Keckhut, P., Duflot, V., Baray, J.-L., Cammas, J.-P., Evan, S., Posny, F., Körner, S. and Bosser, P.:
860 Validation of the Water Vapor Profiles of the Raman Lidar at the Maïdo Observatory (Reunion Island) Calibrated with Global
861 Navigation Satellite System Integrated Water Vapor. *Atmosphere*, 10, 713, 2019

862 Vömel, H., Barnes, J. E., Forno, R. N., Fujiwara, M., Hasebe, F., Iwasaki, S., Kivi, R., Komala, N., Kyrö, E., Leblanc, T.,
863 Morel, B., Ogino, S. Y., Read, W. G., Ryan, S. C., Saraspriya, S., Selkirk, H., Shiotani, M., Canossa, J. V., and Whiteman, D.
864 N.: Validation of Aura Microwave Limb Sounder water vapor by balloonborne Cryogenic Frost point Hygrometer
865 measurements, *J. Geophys. Res.-Atmos.*, 112, D24S37, doi:10.1029/2007JD008698, 2007a.

866 Vömel, H., Naebert, T., Dirksen, R., and Sommer, M.: An update on the uncertainties of water vapor measurements using
867 cryogenic frost point hygrometers, *Atmos. Meas. Tech.*, 9, 3755–3768, <https://doi.org/10.5194/amt-9-3755-2016>, 2016.

868 Witte J. C., Thompson, A. M., Smit, H. G. J., Fujiwara, M., Posny, F., Coetzee, G. J. R., Northam, E. T., Johnson, B. J.,
869 Sterling, C. W., Mohammed, M., Ogino, S.-Y., Jordan, A., daSilva, F. R., and Zainal, Z.: First reprocessing of Southern
870 Hemisphere ADDitional OZonesondes (SHADOZ) profile records (1998–2015) 1: Methodology and evaluation, *J. Geophys.*
871 *Res.*, 122, 6611–6636, <https://doi.org/10.1002/2016JD026403>, 2017.

872 Yan, X., Wright, J. S., Zheng, X., Livesey, N. J., Vömel, H., and Zhou, X.: Validation of Aura MLS retrievals of temperature,
873 water vapour and ozone in the upper troposphere and lower–middle stratosphere over the Tibetan Plateau during boreal
874 summer, *Atmos. Meas. Tech.*, 9, 3547–3566, <https://doi.org/10.5194/amt-9-3547-2016>, 2016.

875 Yuan, W., Geller, M. A. and Love, P. T.: ENSO influence on QBO modulations of the tropical tropopause. *Q. J. Roy. Meteorol.*
876 *Soc.*, 140: 1670-1676. <https://doi:10.1002/qj.2247>, 2014

877 Yulaeva, E. and Wallace, J. M.: The Signature of ENSO in Global Temperature and Precipitation Fields Derived from the
878 Microwave Sounding Unit, *J. Climate*, 7, 1719-1736, [https://doi.org/10.1175/1520-0442\(1994\)0072.0.co;2](https://doi.org/10.1175/1520-0442(1994)0072.0.co;2), 1994

879 Yulaeva, E., Holton, J. R., and Wallace, J. M.: On the Cause of the Annual Cycle in Tropical Lower-Stratospheric
880 Temperatures, *J. Atmos. Sci.*, 51(2), 169-174, 1994.

881 Zhou, X. L., Geller, M. A., and Zhang, M. H.: Tropical cold point tropopause characteristics derived from ECMWF reanalyses

882 and soundings, J. Climate, 14, 1823–1838, [https://doi.org/10.1175/1520-0442\(2001\)0142.0.co;2](https://doi.org/10.1175/1520-0442(2001)0142.0.co;2), 2001.

883 Zhou, X. L., and J. R. Holton: Intraseasonal variations of tropical cold point tropopause temperatures. J. Climate, 15, 1460-
884 1473, 2002

885

886

887

888

889

890

891

892

893

894

895

896

897

898 **Table 1:** CPT properties (temperature and height) from the radiosonde launches on 25 January 2016/3 March 2017 and NDACC/SHADOZ
899 seasonal mean (December-March) CPT properties (for the period 1997-2017).

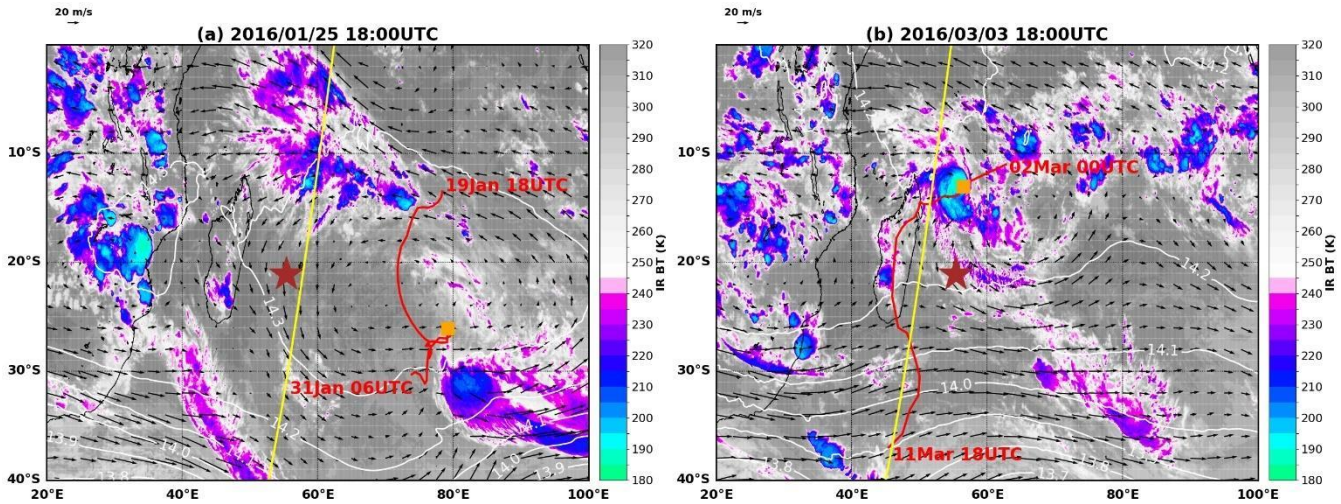
900

	Observations	CPT T (K)	CPT altitude (km)
mean SHADOZ Dec-March (1997-2017)	200	193.90 (± 2.26)	17.31 (± 0.71)
Profile on 25 January 2016	1	192.64	17.30
Profile on 3 March 2017	1	194.58	16.10

901

902

903



904

905

906 **Figure 1:** Infrared (10.8 μm) brightness temperature (K) observed by METEOSAT-7 at the time of the CFH launch for a) 25
907 January 2016 at 18 UTC and b) 3 March 2017 at 18 UTC. The red lines correspond to the best tracks of tropical cyclones
908 Corentin (19-31 January 2016) and Enawo (02-11 March 2017). The orange squares indicate the positions of the TC centers
909 (defined as the minimum pressure in the Météo-France best track data) at the time of the satellite observation. The brown stars
910 indicate the position of the Maïdo Observatory on Réunion Island (21.08°S, 55.38°E). The yellow lines correspond to CALIPSO
911 orbit tracks on 25 January 2016 at 21:06 UTC and 3 March 2017 at 21:41 UTC. Arrows on the maps represent the wind field at
912 150 hPa from the ECMWF analyses at 18 UTC. The white contours indicate ECMWF geopotential heights at 150 hPa.

913

914

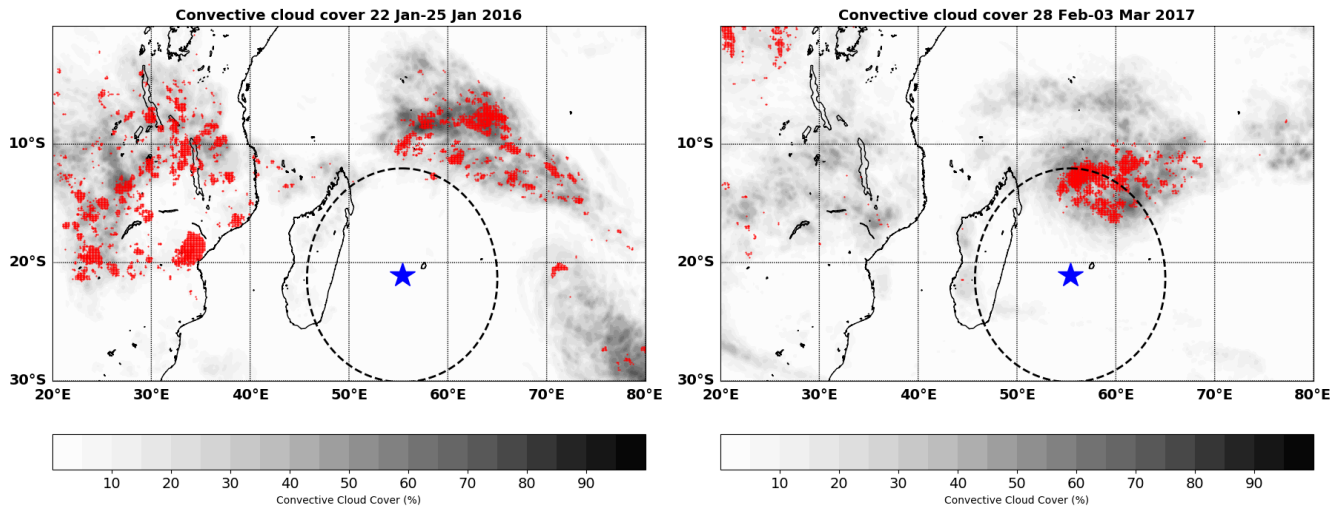
915

916

917

918

919



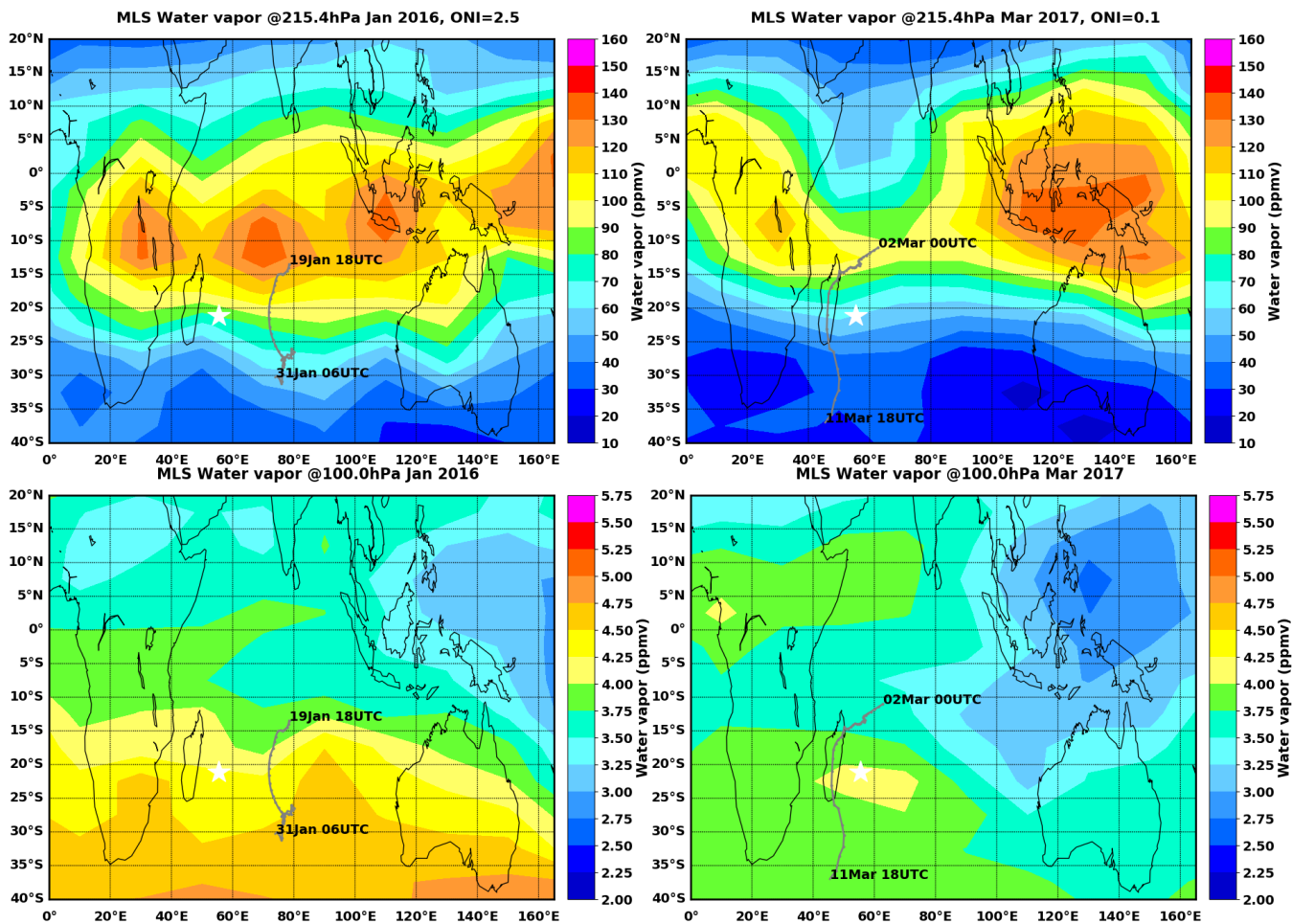
920

921 **Figure 2:** Maps of convective cloud cover (gray shading) computed using 3-hourly data of
 922 METEOSAT 7 infrared brightness temperature at 5 km resolution for 22–25 January 2016
 923 (left) and 28 February–3 March 2017 (right). The red dots indicate pixels with the coldest
 924 tops (≤ 190 K) that capture the deepest part of convection. The dashed circle indicates a
 925 range ring of 1000 km around the Maïdo Observatory (blue star).

926

927

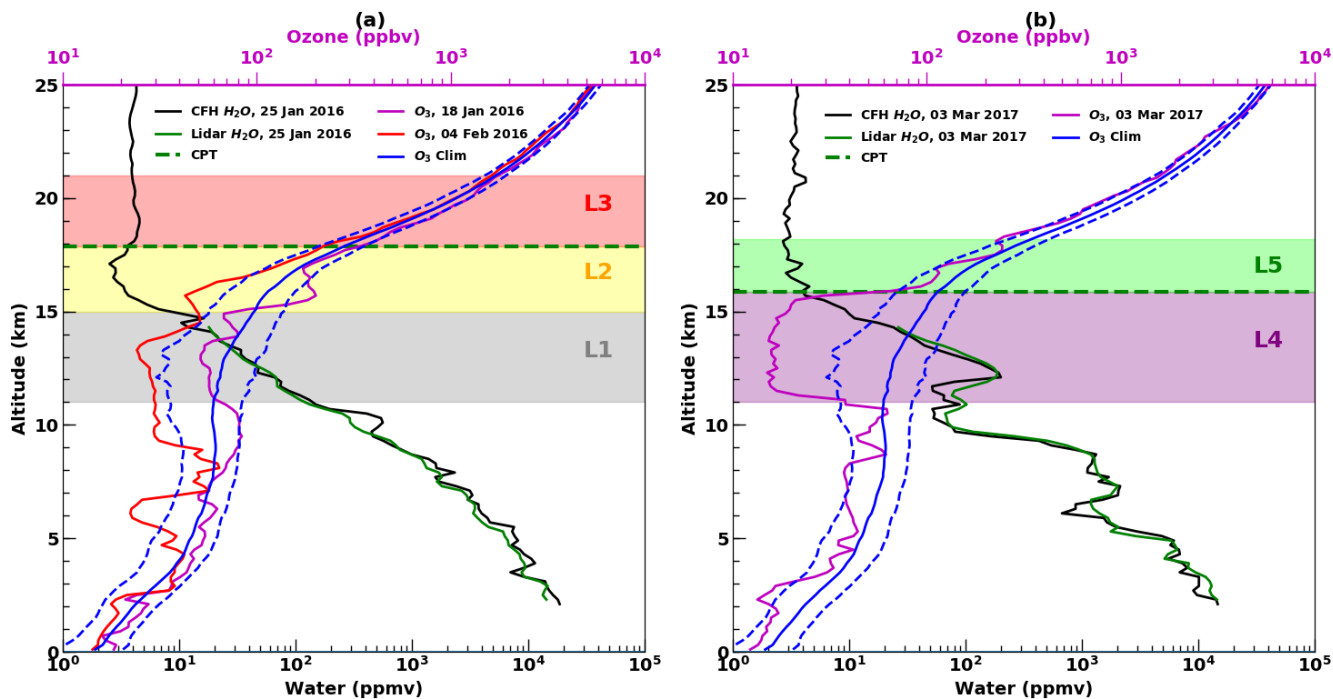
928



929

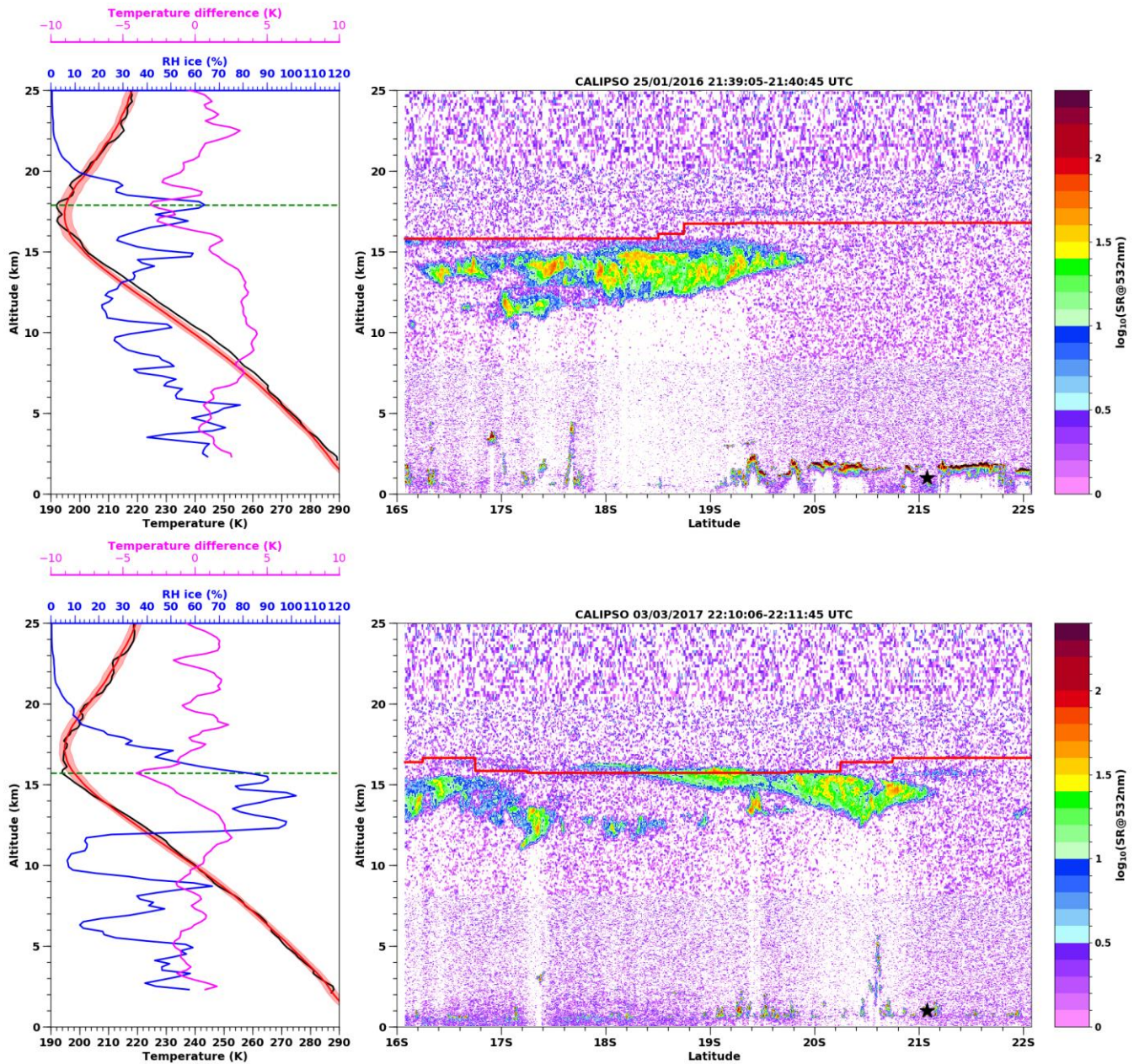
930

931 **Figure 3:** MLS water vapor mixing ratio (ppmv) gridded in the SWOOSH data set at 215 hPa for January 2016 (upper left)
 932 and for March 2017 (upper right). The gray lines correspond to the best tracks of tropical cyclones Corentin (19-31 January
 933 2016) and Enawo (02-11 March 2017). Bottom panels: same as upper panels but for 100 hPa.



934

935 **Figure 4.** Vertical profiles of: a) CFH and lidar water vapor profiles (ppmv) on 25 January 2016 (black and green line
 936 respectively), NDACC/SHADOZ ozone profiles on 18 January 2016 (purple line) and 4 February 2016 (red line); b) CFH and
 937 lidar water vapor profiles (black and green line respectively) and NDACC/SHADOZ ozone profile (purple line) on 3 March
 938 2017. The location of the cold point tropopause is indicated by the dashed green line. Also shown on each plot is the 1998-
 939 2017 climatological mean ozone profile (blue line) for DJFM and the \pm one standard deviation of the climatology corresponds
 940 to the dashed blue line. The most important layers in the water vapor/ozone profiles are shaded and named.



941

942

943

944

945

Figure 5: Top and bottom left: vertical profiles of temperature and relative humidity with respect to ice (black and blue line respectively) measured on 25 January 2016 at 17:52 UTC and 3 March 2017 at 18:00 UTC. The green dashed line corresponds to the cold point tropopause. The NDACC/SHADOZ climatological-mean summertime (DJFM) profile of temperature (red line), the \pm one standard deviation (red shading) and temperature anomaly (magenta line) are also shown. Top and bottom

946 right: Latitude-altitude distribution of CALIOP backscattering ratio at 532 nm along CALIOP track near Réunion Island on
947 25 January 2016 (top right) and 3 March 2017 (bottom right). The mean longitude difference between the CFH profile and the
948 CALIOP track is 2.4° on 25 January 2016 and 5.3° on 3 March 2017. The red curve on each CALIOP plot corresponds to the
949 tropopause height provided by the GEOS 5 global model data available in the CALIPSO Level 1 data files. The latitude of the
950 Maïdo Observatory is indicated by the black star on each CALIOP plot.

951

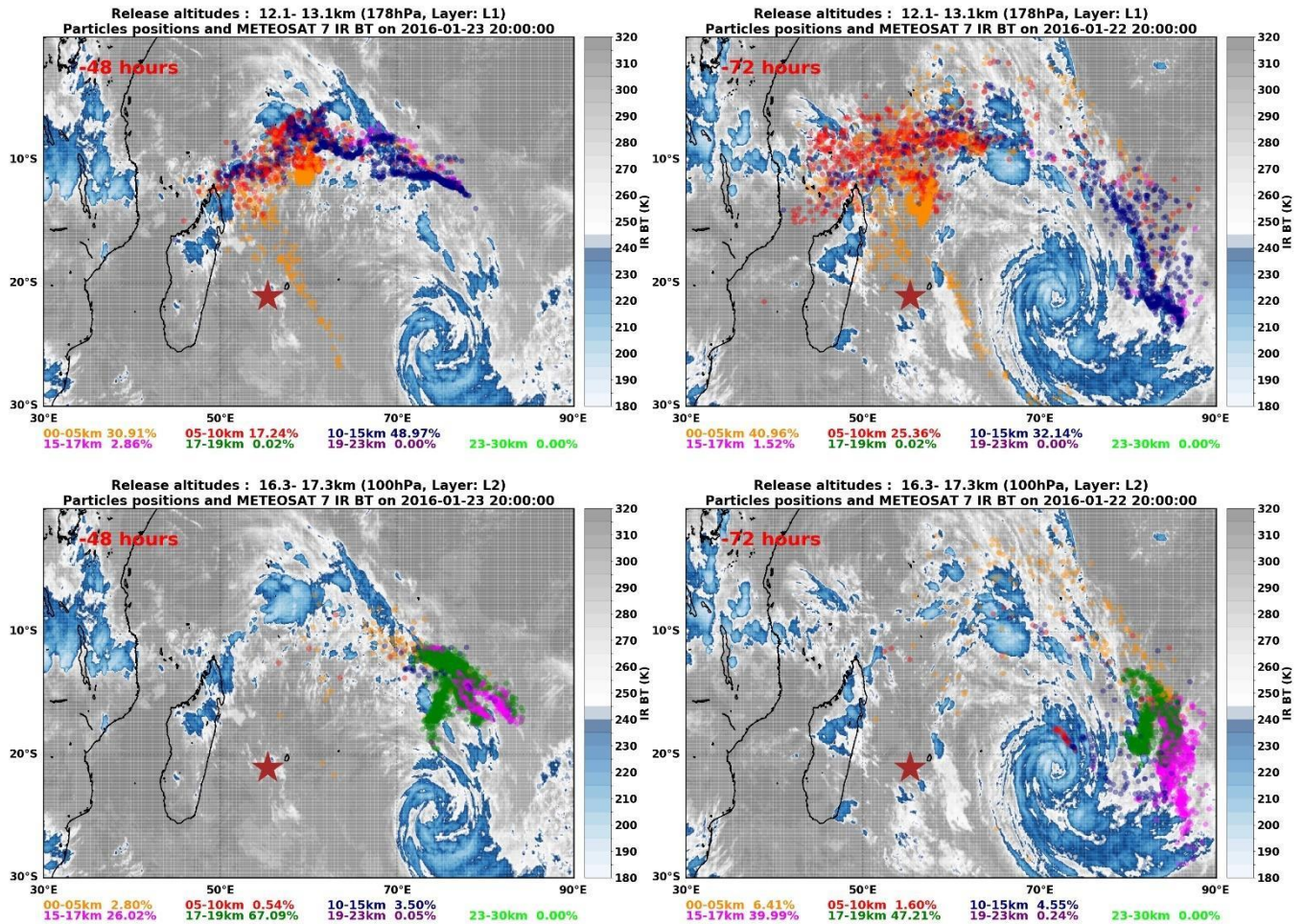
952

953

954

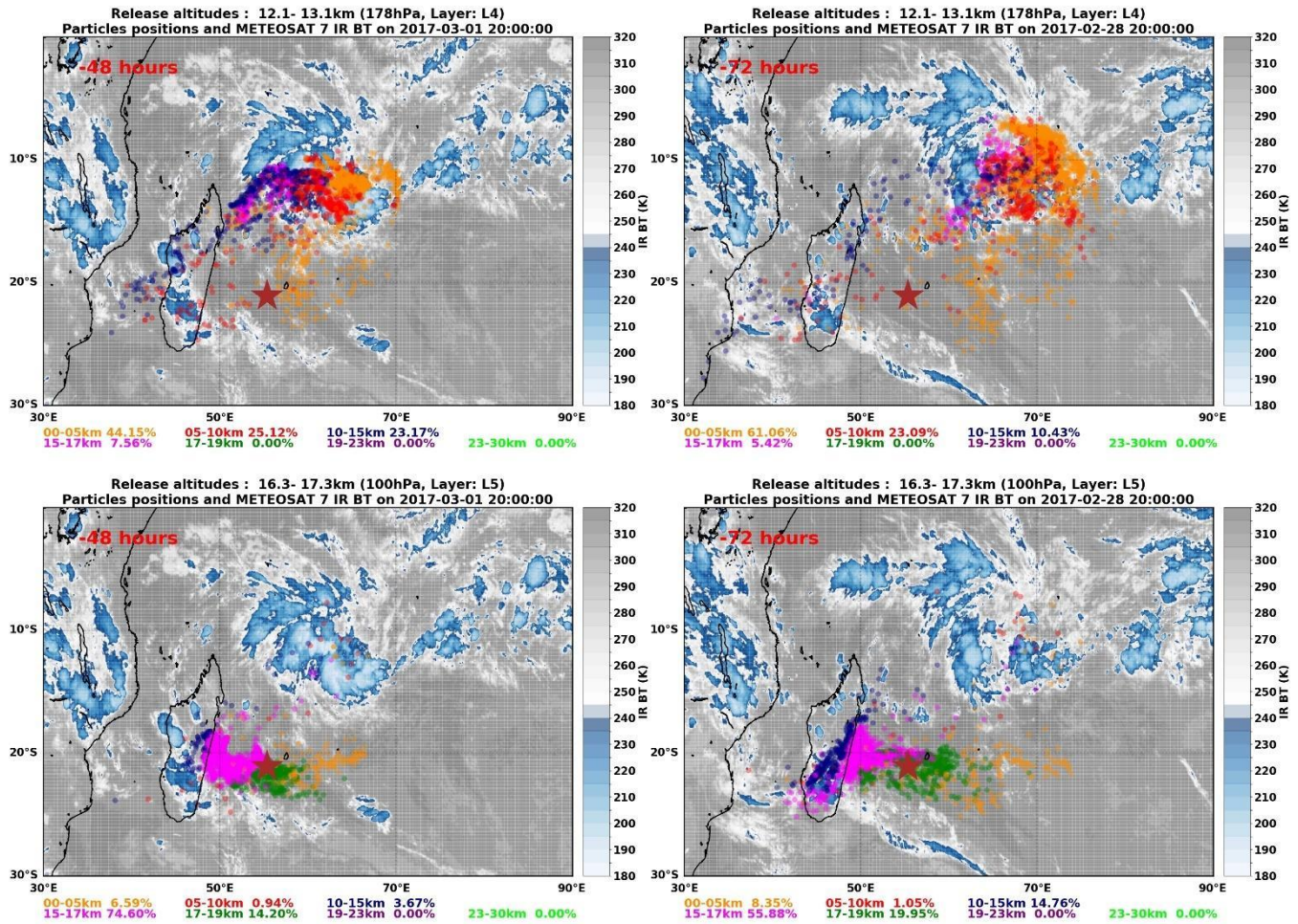
955

956



957

958 **Figure 6:** Backward trajectories calculated with the FLEXPART model for the CFH flight on 25 January 2016. On the upper
 959 panel backward trajectories were initialized at 178 hPa (Layer L1) on 25 January 2016. The particle positions two days before
 960 (on 23 January 2016 at 20 UTC, upper left) and three days before (on 22 January 2016 at 20 UTC, upper right) are shown with
 961 respect to the METEOSAT 7 cloud distribution at those times. The altitude range of the particles (e.g. 0-5km) and the percent
 962 of particles in that altitude range are indicated according to a color code shown on the bottom of each panel. Bottom panel:
 963 same as upper panel but for backward trajectories initialized at 100 hPa (Layer L2) on 25 January 2016.

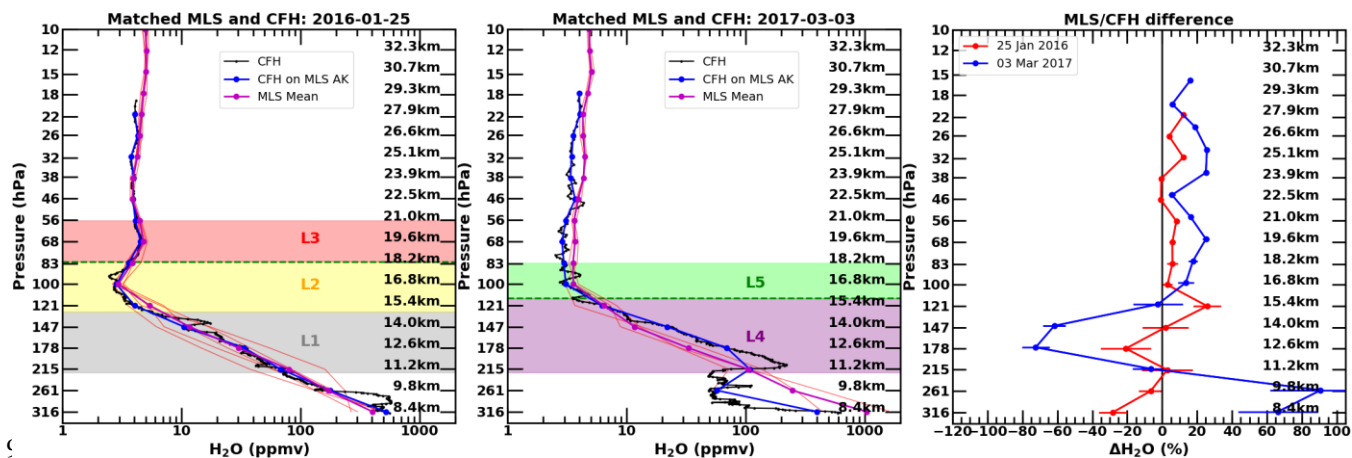


964

965 **Figure 7:** Backward trajectories calculated with the FLEXPART model for the CFH flight on 3 March 2017. On the upper
 966 panel backward trajectories were initialized at 178 hPa (Layer L4) on 3 March 2017. The particle positions two days before
 967 (on 1 March 2017 at 20 UTC, upper right) and three days before (on 28 February 2017 at 20 UTC, upper left) are shown with
 968 respect to the METEOSAT 7 cloud distribution at those times. The altitude range of the particles (e.g. 0-5km) and the percent
 969 of particles in that altitude range are indicated according to a color code shown on the bottom of each panel. Bottom panel:
 970 same as upper panel but for backward trajectories initialized at 100 hPa (Layer L5) on 3 March 2017.

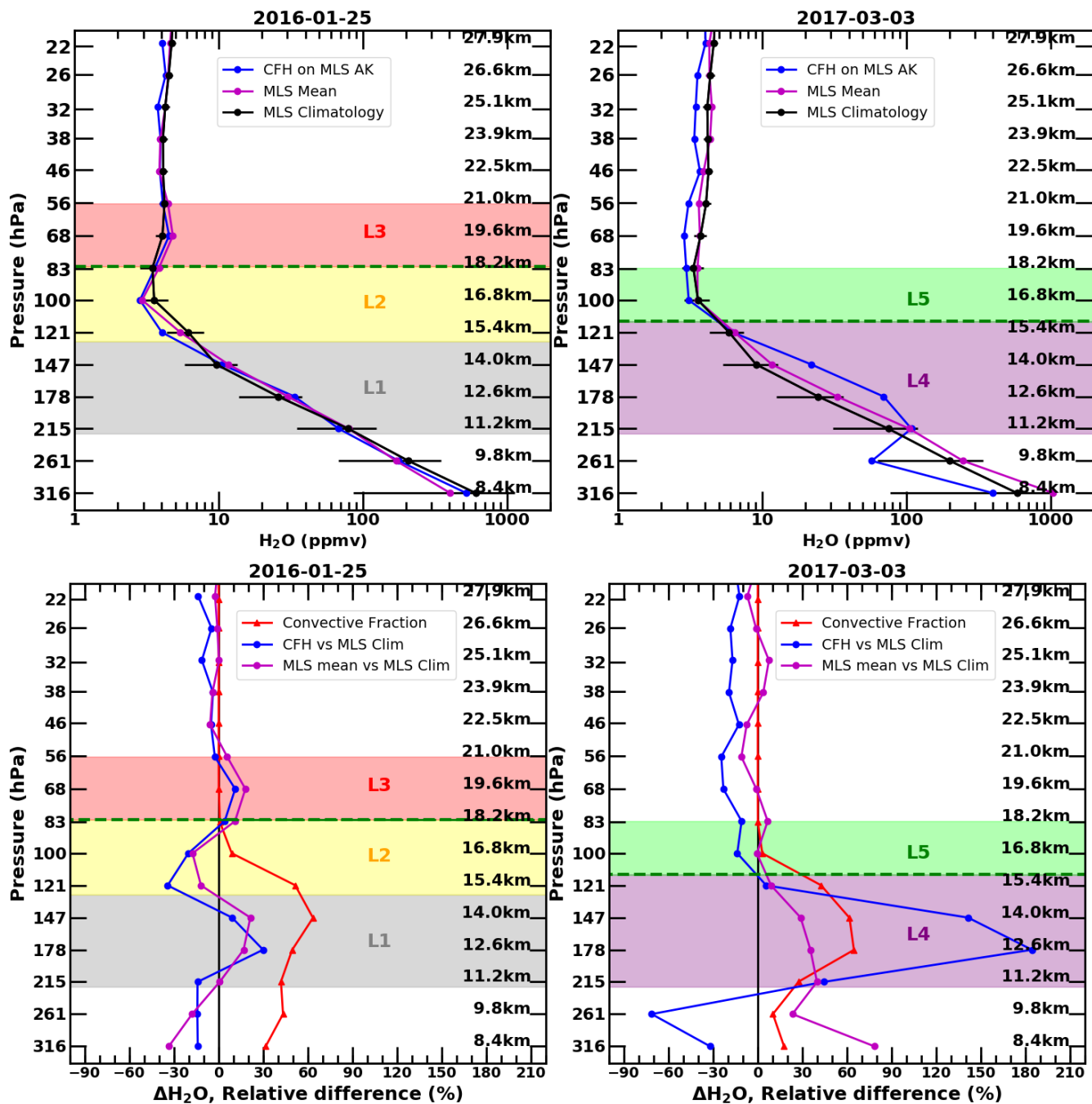
971

972



974

975 **Figure 8:** Left and middle panels: High-resolution (black line) and convolved (blue line) CFH water vapor profiles and closest-
 976 matched MLS profiles (thin red line) on 25 January 2016 (5 profiles) and 3 March 2017 (3 profiles). The mean MLS profile
 977 for each date corresponds to the thick magenta line. The location of the cold point tropopause is indicated by the dashed green
 978 line. Important water vapor features are shaded and named. Right panel: Mean percent difference between the convolved CFH
 979 water vapor profile and MLS coincident profiles on 25 January 2016 (red line) and 3 March 2017 (blue line). The horizontal
 980 bars indicate twice the standard error of the mean percent difference. Markers for each pressure level on 3 March 2017 are
 981 slightly offset in pressure for clarity. Corresponding altitude values for MLS pressure levels are also shown on each plot.



982

983 **Figure 9:** Upper panel: Convolved CFH water vapor profiles (blue line), mean of closest-matched MLS profiles (magenta)

984 and monthly mean climatological MLS water vapor profile for Réunion Island (black line, see text for definition of the MLS

985 climatological profile) on 25 January 2016 (upper left) and 3 March 2017 (upper right). The horizontal bars in black correspond
986 to the \pm one standard deviation range. Bottom panel: Relative difference between the convolved CFH water vapor profile and
987 the MLS climatological profile for Réunion Island (blue line) and the mean of closest-matched MLS profiles and the MLS
988 climatological profile (magenta line). The convective fraction computed with FLEXPART backtrajectories and METEOSAT
989 7 infrared brightness temperature is shown in red. Corresponding altitude values for MLS pressure levels are also shown on
990 each plot.